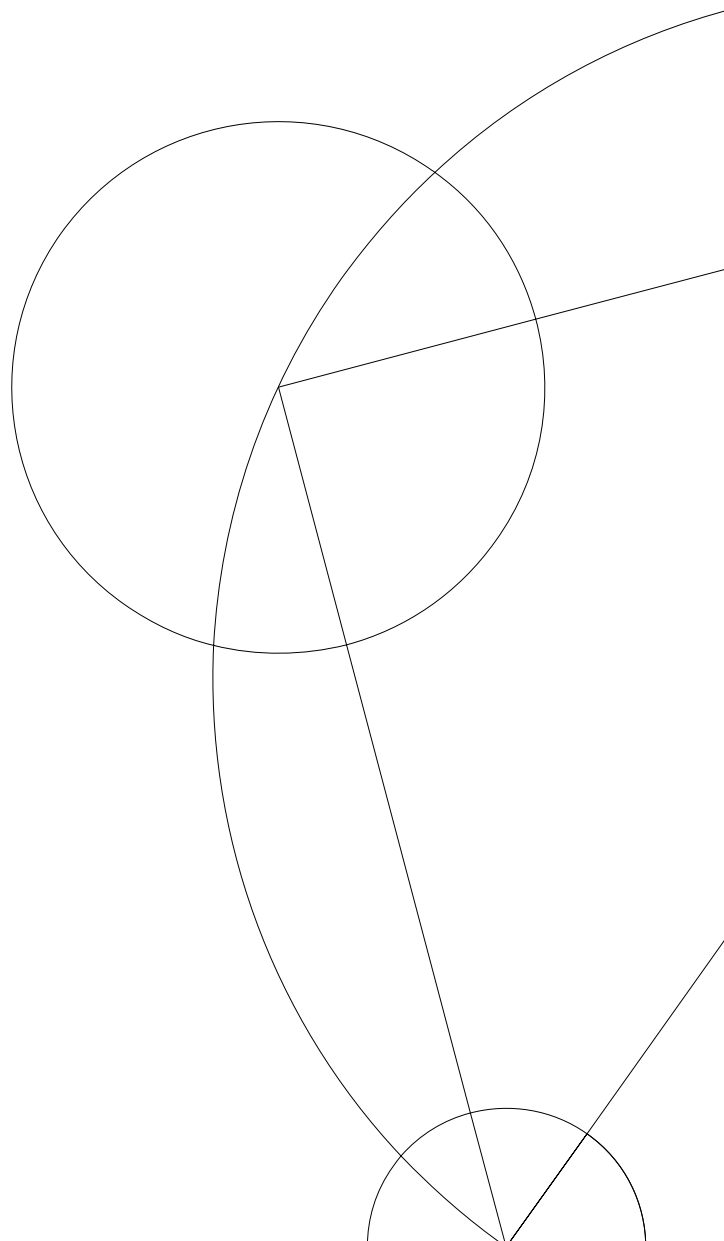**Master's Thesis in Physics**

Søren Birkemose

Polarized Neutron Reflectometry investigation of SC-FMI-SM Heterostructures

Supervisors:

Kim Lefmann, NBI

Peter Krogstrup, NBI

Submitted: February 1, 2023

Acknowledgements

I would like to thank my supervisors Kim Lefmann and Peter Krogstrup, for guidance through this project. I would also like Alessandra Luchini and Malvika Tripathi for help with analysing the data, and discussion. I would like to thank Thomas Saerbeck the instrument responsible at ILL, who do to Covid-19 ended up doing some of the experiments for us. Last I would like to thank my research group for support, feedback and fun.

Abstract

Topological qubits are an area of great interest in quantum computing, as such a system would be more stable than using trapped quantum particle. One possible methods of creating these, is through the use quasiparticle Majorana fermions, which are amongst others places hypothesised to exist in p-wave superconductors. While no single material is known to be a p-wave superconductor, such a system might be present in a thinfilm made of a superconductor (SC), a ferromagnetic insulator (FI) and a semiconductor (SM) with a strong spin-orbit coupling. To test these films, polarized neutron reflectometry (PNR) is a useful tool as it be used to detect determine the magnetization in the different layers of the film. We have in this project used PNR to test samples composed of InAs (SM), EuS (FI) and Pb (SC) in order to determine wether they exhibit the conditions necessary for a p-wave superconductor. While we do find the presence of a magnetic field in the InAs layer, we cannot definitively determine whether these system exhibits the conditions of a p-wave superconductor.

Contents

1 Introduction

In 1985 Richard Feynmann theorized about the possibility of creating bits the size of atoms, and thereby introducing the concept of quantum computation [3]. One of the biggest obstacles to overcome in building a large scale quantum computer, is the controlling of errors, as small perturbations can cause the system to decohere. As such we are interested in finding a way, to create a system of qubits that are more stable, even on larger scales. One theoretical solution, is a so called topological quantum computer, where in the qubits would be composed of quasiparticle Majorana fermions. Majorana fermions are particles which are their own anti-particles. While there currently is no know elementary particles which are Majora fermions (MF), they are expected to exist as a quasiparticle excitation of certain condensed matter system. As Majorana fermions in such a system are non-abelian anyons, they have the exchange statistics necessary for topological quantum computing [32]. As a Majorana fermion in a condensed matter system is its own whole, it must be composed of a superposition of an electron and a hole state. As the wavefunctions of the Boguliubov quasiparticles in superconducting systems have both an electron and a hole component, it is logical to search for MF excitations in such systems. However while the condition for MF excitations, are not met in normal s-wave superconductors, where the Cooper pairs are formed of electrons with opposite spin projections (a singlet paring), they are likely to be met in spinless superconducting systems with triplet pairing, so called p-wave superconductors. While existence of p-wave superconductor, has never been experimentally observed, Majorna Fermion are topologically invariant, and should therefore exist in systems with similar properties to a p-wave superconductor. A system of p-wave superconductivity may be achieved in a semiconductor system, when brought into tunneling contact with a superconductor. The strong spin orbit coupling results in a momentum dependent band splitting. Furthermore by coupling the semiconductor with a ferromagnetic insulator, the Zeeman splitting lifts the degeneracy resulting in a spinless triplet pairing of electrons.

In this project we have created a thin film, composed of Indium Arsenide (semiconductor), Europium Sulfide (ferromagnetic insulator) and lead (superconductor). Using neutron reflectometry, we will examine whether the proximity effect, results in a magnetic coupling

inside the semiconductor. We find the presence of a magnetization in the semiconducting layer, which seems to be affected by the presence of superconductivity in the lead layer.

2 Theoretical Background

2.1 Superconductivity

Unlike normal conductivity of electrons which comes from the valence electrons ability to move more or less freely through a lattice of ions, superconductivity arises from the formation of Coopers pairs, mediated by some kind of bosons. We will here give a short introduction, on some of the basics regarding superconductivity that is relevant, for our project. This section is based on the textbooks [6, 17, 25, 47]

2.1.1 Formalism

Due to its convenience when regarding many body systems, we will be using the formalism of second quantization in this section. In this language we ask how many particles there are in each state, instead of the state of the individual particles. Consider the electron state $\psi_{\mathbf{k},\sigma}(r)$, where $\mathbf{k}$ is the momentum and σ is the spin of the electron. We start by defining the creation operator $c_{\mathbf{k},\sigma}^{\dagger}$, which create a state of an electron, in a plane or Bloch wave, with the quantum number $(\mathbf{k}, \sigma)$, and the annihilation operator $c_{\mathbf{k},\sigma}$ which destroys such a state. Taking into account that the electrons follow the Pauli exclusion principle, we postulate the following anti-commutation relation:

$$\{c_{\mathbf{k},\sigma}, c_{\mathbf{k}',\sigma'}^{\dagger}\} = \delta_{\mathbf{k},\sigma}\delta_{\mathbf{k}',\sigma'} \tag{2.1}$$

In this formalism, the occupation number of a state is the given by the number operator $n_{\mathbf{k},\sigma} = c_{\mathbf{k},\sigma}^{\dagger}c_{\mathbf{k},\sigma}$.

We now consider a Fermi gas of non-interacting electrons. The Hamiltonian of such a system is then given as a sum of the energy of the individual states $\epsilon_{\mathbf{k},\sigma}$, multiplied with the number operator of said state:

$$H = \sum_{\mathbf{k},\sigma} \epsilon_{\mathbf{k},\sigma} c_{\mathbf{k},\sigma}^{\dagger} c_{\mathbf{k},\sigma} \tag{2.2}$$

3

For free electrons the energy is given by:

$$\epsilon_{\mathbf{k}} = \frac{\hbar^2 \mathbf{k}^2}{2m} \tag{2.3}$$

As electrons are fermions, the probability that a state of a given energy ϵ will be occupied is given by the Fermi-Dirac distribution:

$$f(\epsilon) = \frac{1}{e^{(\epsilon-\mu)/k_B T} + 1} \tag{2.4}$$

With μ being the chemical potential, which is found from the requirement that the density of electrons per unit volume is:

$$\frac{N}{V} = \frac{2}{(2\pi)^3} \sum_n \int \frac{1}{e^{(\epsilon_{n\mathbf{k}}-\mu)/k_B T}} d^3 k \tag{2.5}$$

Where the factor 2 comes from the assumption that the energies $\epsilon_{\mathbf{k}}$ are independent of the spin state, giving us two allowed values for each value of $\mathbf{k}$ and n are the electron bands. By taking the ground state of the system ($T \to 0$), we then define the Fermi energy ϵ_F as being the value of the topmost filled state. If we represent the occupied states as point in a sphere in $\mathbf{k}$-space, then the Fermi energy will be the energy at the surface, and we define the magnitude of that wavevector at the surface as the Fermi vector, see fig.. The Fermi energy is then:

$$\epsilon_F = \frac{\hbar^2}{2m} k_F^2 \tag{2.6}$$

where k_F for a system of N free electrons is given as $k_F = (\frac{3\pi^2 N}{V})^{1/3}$. Furthermore we also define the density of states $D(\epsilon) = \frac{dN}{d\epsilon}$, which is the number of states per unit energy range, which for a free Fermi gas is:

$$D(\epsilon) = \frac{dN}{d\epsilon} = \frac{V}{2\pi^2} (\frac{2m}{\hbar^2})^{3/2} \cdot \epsilon^{1/2} = \frac{3N}{2\epsilon} \tag{2.7}$$

2.1.2 Cooper Pairs

The first microscopic theory of superconductivity was published by Bardeen, Cooper and Schrieffer in 1957 [7], and is called the BCS theory. It is build upon a few key ideas, the most important being the existence of an effective attractive potential, between electrons near the Fermi surface. The attractive potential between electrons comes from the electron-phonon interaction with the crystal lattice [6]. As shown in fig 2.1, an electron in the state $\psi_{\mathbf{k},\sigma}$ can excite a phonon with crystal momentum $\hbar\mathbf{q}$, leaving the electron in the state $\psi_{\mathbf{k}',\sigma}$ with $\mathbf{k}' = \mathbf{k} - \mathbf{q}$. This phonon can then be absorbed by another electron which picks up
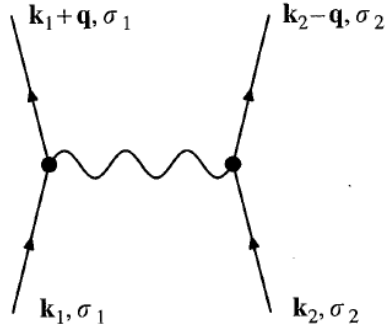
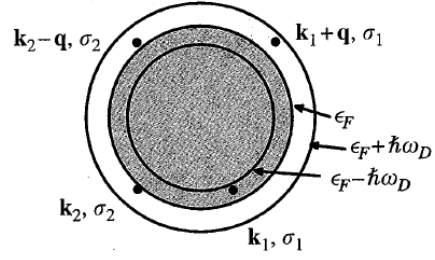**Figure 2.1:** Feynman diagram of the an electron exciting a phonon [6]

Figure 2.2: Electron lying with in $\hbar\omega_D$ of the Fermi surface, can form Cooper Pairs. [6]

the momentum $\hbar\mathbf{q}$. The resulting momentum transfer results in an effective interaction between the two electrons.

$$V_{\text{eff}}(\mathbf{q}, \omega) = |g_{\mathbf{q}}|^2 \frac{1}{\omega^2 - \omega_D^2} \tag{2.8}$$

which is simplified to:

$$V_{\text{eff}}(\mathbf{q}, \omega) = |g_{\text{eff}}|^2 \frac{1}{\omega^2 - \omega_D^2} \tag{2.9}$$

where g_{eff} is a constant and ω_D is the Debye frequency of the phonons. As we can see $V_{\text{eff}}(\mathbf{q}, \omega)$ results in an attractive interaction when $\omega < \omega_D$. As the temperatures of interest for superconductivity is very small, we are in the regime where $\hbar\omega_D \gg k_B T$. We therefore assume the simple form

$$V_{\text{eff}} = |g_{eff}|^2 \quad \omega < \omega_D \tag{2.10}$$

The Hamiltonian, for the electron-electron interaction then becomes:

$$H = -|g_{\text{eff}}|^2 \sum c_{\mathbf{k}+\mathbf{q},\sigma}^\dagger c_{\mathbf{k}'-\mathbf{q},\sigma'}^\dagger c_{\mathbf{k},\sigma} c_{\mathbf{k}',\sigma'} \tag{2.11}$$

where the sum is over all values of $\mathbf{k}, \sigma, \mathbf{k}', \sigma'$ and $\mathbf{q}$ with the restriction, that the electron energies are within $\hbar\omega_D$ of the Fermi surface [6].

Now the presence of this attraction between electrons doesn't mean that there is an effective attractive potential, but combined with effects that reduce the Coulomb repulsion between the electrons, such as screening, it is possible to achieve a situation with an effective attraction between electron near the Fermi surface resulting in Cooper pairs, see fig. 2.2 [6, 17].

2.2 Majorana Fermions

As adressed in ch. 1 Majorana fermions (MF) are fermionic particles which are their own anti-particles. So far no known elementary particles are their own anti-particles. Majorana fermions are however in likely to exist as quasiparticle excitation in certain condensed matter systems, this being electron systems with a fermisurface, where the MF would be a quasiparticle with its "own hole" [32]. A MF is in a sense half a fermion, meaning any fermionic state could be described as a superposition of two MFs. For a normal fermion this is simply a mathematical operation whereby the fermion is split up into a real and an imaginary part. This splitting has no physical consequences, as the two MFs are spacially localized close to one another, overlap and cannot be addressed individually. The MFs we are looking for in this project, are fermionic states that each can be described as a superposition of two MFs that are spatially separated (or prevented from overlap in some other manner). As the MF is it own hole, it must be an equal superposition of an electron and a hole state. Therefore is makes sense to look for such an excitation in superconducting systems, where the wave function of the Bogoliubov quasiparticle has both an electron and a hole component. In most common superconductors, the Cooper pairs are formed of two electrons with opposite spin (forming a singlet state), this type of paring is called s-wave, and the annihilation operator of its Bogoliubov quasiparticle is:

$$b = uc_\uparrow^\dagger + vc_\downarrow \tag{2.12}$$

where c_σ annihilates a fermion with spin projection $\sigma = \uparrow, \downarrow$. The MF having equal electron and hole components will instead have an annihilation operator:

$$\gamma = uc_\sigma^\dagger + u^* c_\sigma \tag{2.13}$$

Which is hermitian so $\gamma = \gamma^\dagger$ and in contrast to the s-wave operator have equal spin projections. Now such quasiparticles don't occur in most superconductors, however isolated MFs might occur in vortices and on edges of effectively spinless superconducting systems with triplet pairing. For a one dimensional superconducting system this is called p pairing symmetry and for a two dimensional system it is $p_x \pm ip_y$. Below we will look at why MF's should be present, and how such systems might be created. Most of this section is based on [32].

2.2.1   Majorana Fermions in a p-wave superconductor

If we imagine that we have a 1 dimensional tight-binding chain with *p*-wave superconducting pairings, then the Hamiltonian of such a system would be:

$$H_{chain} = \sum_{i=1}^{N}(-\mu c_i^\dagger c_i) + \sum_{i=1}^{N-1}(-t(c_i^\dagger c_{i+1} + c_{i+1}^\dagger c_i) + \Delta c_i c_{i+1} + \Delta^* c_i^\dagger c_{i+1}^\dagger) \quad (2.14)$$

Where c_i is the annihilation operator acting on site i and $c_i^\dagger c_i = n_i$ is the number operator. Also μ is the chemical potential, t is the hopping amplitude, and $\Delta = |\Delta|e^{i\phi}$ is the superconducting gap, with all three assumed to be independent of sites. We can then choose the superconducting phase ϕ to be zero so that $\Delta = |\Delta|$. It should be noted that we have left out the spin orientation, since we only consider one value of the spin orientation. Our *p*-wave superconductor consist of pairings of electrons with the same spin orientation, as opposed to the normal *s*-wave which pairs electrons with opposite spin. We now introduce Majorana operators by splitting the fermion operators into a real and an imaginary part, as mentioned above:

$$c_i = \frac{1}{2}(\gamma_{i,1} + i\gamma_{i,2}) \quad (2.15a)$$

$$c_i^\dagger = \frac{1}{2}(\gamma_{i,1} - i\gamma_{i,2}) \quad (2.15b)$$

where $\gamma_{i,j}$ are Majorana operators on site *i*. That they indeed are Majorana operators, can be show by inverting them:

$$\gamma_{i,1} = c_i^\dagger + c_i \quad (2.16a)$$

$$\gamma_{i,2} = i(c_i^\dagger - c_i) \quad (2.16b)$$

Which are obviously hermitian, $\gamma^\dagger = \gamma$, and hence they are Majorana operators. Now if we set $t = |\Delta| = 0$ and $\mu < 0$ then the Hamiltionian becomes:

$$H_{chain} = \frac{-i\mu}{2} \sum_{i=1}^{N}(\gamma_{i,1}\gamma_{i,2} + 1) = -\mu \sum_{i=1}^{N} c_i^\dagger c_i \quad (2.17)$$

Where the fermions on each site is simply split up into pairs of Majorana operators as seen in the upper panel of figure 2.3. However if we set $\mu = 0$ and $t = |\Delta| > 0$, then the Hamiltonian becomes:

$$H_{chain} = -it \sum_{i=1}^{N-1} \gamma_{i,2}\gamma_{i+1,1} \quad (2.18)$$
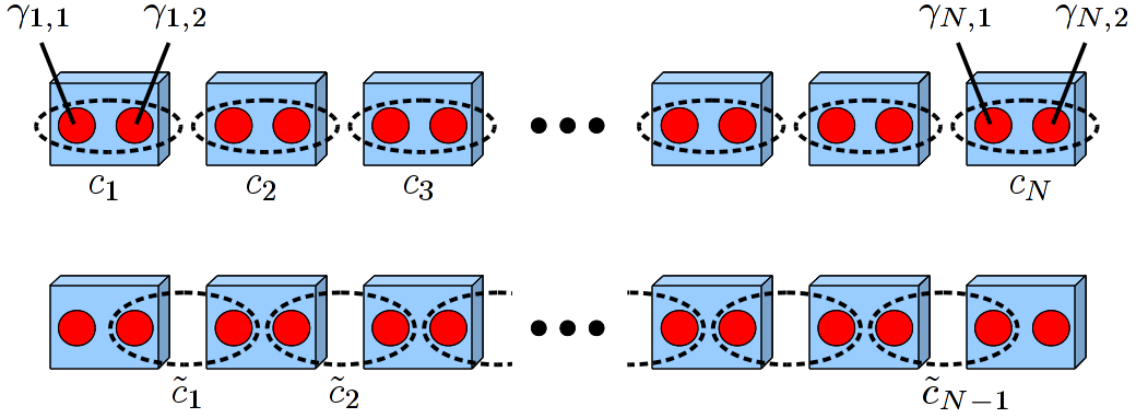
Figure 2.3: Sketch of Kitaev's 1D p-wave superconducting chain. Upper panel: Fermion operators on site i are split into two Majorana fermions, $\gamma_{i,1}$ and $\gamma_{i,2}$. Lower panel: At $\mu = 0$ and $t = \Delta$, the Majoran fermions, pairs with a neighboring site γ_{i+1} and $\gamma_{i,2}$, leaving two unpaired Majorana fermions at $\gamma_{1,1}$ and $\gamma_{N,1}$, which can combine to form a zero energy, highly non-local fermion operator $\tilde{c}_M$ [32]

Where we now end up with a situation where the Majorana operators are paired on neighboring sites as seen in figure 2.3. We can go back to a fermionic representation, by creating a new fermion operator $\tilde{c}_i = (\gamma_{i+1,1} + i\gamma_{i,2})/2$, which pairs Majorana operators on neighboring site, and from which we get that $-\gamma_{i,2}\gamma_{i+1,1} = 2\tilde{c}_i^\dagger \tilde{c}_i = 2\tilde{n}_i$, so eq. 2.18 becomes:

$$H_{chain} = 2t \sum_{i=1}^{N-1} \tilde{c}_i^\dagger \tilde{c}_i \tag{2.19}$$

So $\tilde{c}_i$ and $\tilde{c}_i^\dagger$ are the annihilation and creation operators corresponding to the eigenstates, and the energy cost of making a $\tilde{c}_i$ fermion is $2t$. What is special about this case is that the Majorana operators $\gamma_{1,1}$ and $\gamma_{N,2}$ at each end of the chain, is missing from eq. 2.18. These two state can be combined into the fermionic state:

$$\tilde{c}_M = \frac{1}{2}(\gamma_{N,1} + i\gamma_{1,1}) \tag{2.20}$$

Which is a higly non-localized state, as the Majorana operators are on opposite ends of the chain, see fig 2.3. Furthermore, this state requires zero energy, as the fermion operator is not present in the Hamiltonian. So the Hamiltonian 2.2.1 allows for an odd number of quasiparticles at zero energy cost, and so the ground state is two-fold degenerate corresponding to having an even or odd number of electrons in the superconductor, corresponding to the eigenvalue of the zero energy fermion $\tilde{n_M} = \tilde{c_M}^\dagger, \tilde{c_M} = 0(1)$, for an even or odd number of electrons. While we have only argued for the case where $\mu = t$, it can be shown that the Majorana end states, are present as long as $|\mu| < 2t$ [24]. In two dimensions, similar effects are present [4, 5, 41, 42] but their description becomes more

tedious, and is not really relevant for this project. The Hamiltonian for the continuum version of the 1D and 2D *p*-wave superconductor are:

$$H_{1D} = \int \Psi(\mathbf{x})^\dagger (\frac{\mathbf{p_x}^2}{2m} - \mu)\Psi(\mathbf{x}) + \Psi(\mathbf{x})|\Delta|e^{i\phi}(p_x)\Psi(\mathbf{x}) + h.c.\, \mathrm{d}x \qquad (2.21a)$$

$$H_{2D} = \int \Psi(\mathbf{r})^\dagger (\frac{\mathbf{p}^2}{2m} - \mu)\Psi(\mathbf{r}) + \Psi(\mathbf{r})|\Delta|e^{i\phi}(p_x \pm ip_y)\Psi(\mathbf{r}) + h.c.\, \mathrm{d}r \qquad (2.21b)$$

Where $\Psi(\mathbf{r})^\dagger$ is the real space creation operator, m is the effective mass of the electrons, $h.c.$ is the hermitian conjugate and the superconducting phase ϕ has been reintroduced. Now all we need is the realization of a p or $p_x \pm ip_y$ -wave superconductor.

2.2.2 Proximity induced superconductivity

Instead of looking for a material that would be a p or $p_x \pm ip_y$-wave superconductor, we will instead look for a way to engineer such a pairing in a semiconductor, via proximity induced superconductivity. Recent works suggests [5, 32] that a p-wave superconductor, similar to the Kitaev toy model, can be engineered with three simple components: A 1 dimensional semiconducting wire with a strong spin-orbit coupling, a conventional s-wave superconductor, and a magnetic field perpendicular to to SC surface. The basic layout can be seen in 2.4. By putting our semiconductor and superconductor in close proximity to
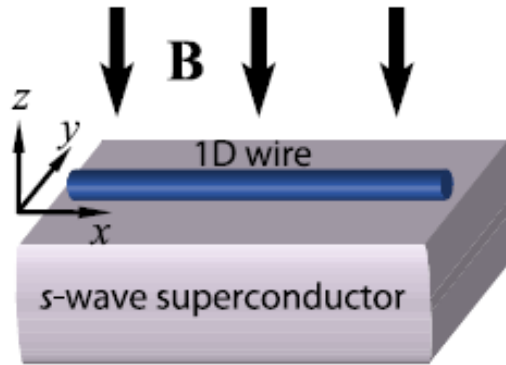
Figure 2.4: Basic sketch for engineering topological superconductivity in a 1D semiconductor with strong spin-orbit coupling. [5]

one another, it becomes possible for electrons to tunnel between these two system. As a result, the electrons in the semiconductor will feel a "proximity induced" superconducting pairing field, the strength of which depends on the superconductor, the semiconductor and the interface between the two. The total Hamiltonian of this system of a semiconductor

with superconductivity can be described by the Hamiltonian:

$$\mathcal{H} = \mathcal{H}_0 + \mathcal{H}_\Delta \tag{2.22}$$

Neglecting electron–electron interactions our semiconductor system $\mathcal{H}_0$ is:

$$\mathcal{H}_0 = \sum_{\sigma=\uparrow,\downarrow} \int \Psi_\sigma^\dagger(\mathbf{r}) H_0(\mathbf{r}) \Psi_\sigma(\mathbf{r}) \mathrm{d}r \tag{2.23}$$

Where $\Psi_\sigma^\dagger(\mathbf{r})$ creates an electron with spin $\sigma = \uparrow, \downarrow$ at the position $\mathbf{r}$. The Hamiltonian $H_0(r)$ is the first quantization single particle Hamiltonian, which for our wire, assuming a Rashba spin-orbit coupling and that the chemical potential is tuned to a regime where only a single 1D subband is occupied, and with $\hbar = 1$, takes the form:

$$H_0 = -\frac{\partial_x^2}{2m} - \mu - i\alpha(\partial_x \sigma_y) + E_Z \sigma_z \tag{2.24}$$

Where m is the effective electron mass, $\alpha \geq 0$ is the strength of the Rashba spin-orbit coupling whitch favors aligning the spins in the y axis, σ_y, σ_z are Pauli spin matrices, and $E_Z = -\frac{1}{2}g\mu_B B_z$ is the Zeeman energy associated with the magnetic field B_z applied in the z direction. With μ_B being the Bohr magneton, and g the Landé g-factor. It is only the magnetic field component which is orthogonal to the spin-orbit field, which will induce topological superconductivity..

The second term in 2.22 is the superconducting paring effect $\mathcal{H}_\Delta$, which we simply include as a phenomenological Hamiltonian:

$$\mathcal{H}_\Delta = \int (\Psi_\downarrow(\mathbf{r}) \Delta(\mathbf{r}, \mathbf{r}') \Psi_\uparrow(\mathbf{r}') + h.c) \mathrm{d}r \mathrm{d}r' \tag{2.25}$$

With $\Delta(\mathbf{r}, \mathbf{r}')$ being the superconducting gap inside the semiconductor, which induces a singlet pairing between electrons of opposite spin. To include both the electrons and the holes, we now introduce the four component Nambu spinor:

$$\bar{\Psi}(\mathbf{r}) = \begin{pmatrix} \Psi_\uparrow(\mathbf{r}) \\ \Psi_\downarrow(\mathbf{r}) \\ \Psi_\downarrow^\dagger(\mathbf{r}) \\ -\Psi_\uparrow^\dagger(\mathbf{r}) \end{pmatrix} \tag{2.26}$$

We can then write 2.22 in the BdG form:

$$\mathcal{H} = \frac{1}{2} \int \bar{\Psi}^\dagger(\mathbf{r}) [\bar{H}_0(\mathbf{r})\delta(\mathbf{r} - \mathbf{r}') + \bar{\Delta}(\mathbf{r}, \mathbf{r}')] \bar{\Psi}(\mathbf{r}) \mathrm{d}r \mathrm{d}r' \tag{2.27}$$

where

$$\bar{H}_0(\mathbf{r}) = \begin{pmatrix} H_0(\mathbf{r}) & \hat{0}_\sigma \\ \hat{0}_\sigma & -\sigma_y H_0^*(\mathbf{r})\sigma_y \end{pmatrix} \tag{2.28a}$$

$$\bar{\Delta}(\mathbf{r},\mathbf{r}') = \begin{pmatrix} \hat{0}_\sigma & \Delta(\mathbf{r},\mathbf{r}')\hat{1}_\sigma \\ \bar{\Delta}^*(\mathbf{r},\mathbf{r}')\hat{1}_\sigma & \hat{0}_\sigma \end{pmatrix} \tag{2.28b}$$

Which are both 4×4 matrices, as $H_0(\mathbf{r})$ is a 2×2 and $\hat{0}$ and $\hat{1}$ are the zero and unit matrices in spin space. The term $-\sigma_y H_0^*(\mathbf{r})\sigma_y$ is the time reversal of $H_0(\mathbf{r})$, and appears because holes are time-reversed electrons. The excitation spectrum of eq 2.27, is found by solving the Bogoliubov-de Gennes equation, for the four component eigenstate $\bar{\Phi}_i(\mathbf{r})$:

$$\bar{H}_0(\mathbf{r})\bar{\Phi}_i(\mathbf{r}) + \int \bar{\Delta}(\mathbf{r},\mathbf{r}')\bar{\Phi}_i(\mathbf{r}')\mathrm{d}r' = E_i\bar{\Phi}_i(\mathbf{r}) \tag{2.29}$$

resulting in the Hamiltonian:

$$\mathcal{H} = \frac{1}{2}\sum_i E_i \Psi_i^\dagger \Psi_i \tag{2.30}$$

with

$$\Psi_i = \int \bar{\Phi}_i(\mathbf{r}) \cdot \bar{\Psi}(\mathbf{r})\mathrm{d}r \tag{2.31}$$

By explicitly including the hole states we doubled the dimensions of the Hamiltonian, which results in an artificial doubling of the eigenstates. There must then be some symmetry relation between the eigenstates so that the number of independent solutions remains unchanged. This symmetry is the electron-hole symmetry, which has the operator

$$P = CK = \tau_y \otimes \sigma_y K \tag{2.32}$$

Where K is the operator for complex conjugation, C is the charge conjugate and τ_i are the Pauli matrices in electron-hole space, with the resulting Kronecker product $\tau_i \otimes \sigma_i$, being a 4×4 matrix. It can then be shown that:

$$P\mathcal{H}P^\dagger = -\mathcal{H} \tag{2.33}$$

So if $\bar{\Phi}_i(\mathbf{r})$ and Ψ_i are solutions with positive energy, then there is also a solutions $\bar{\Phi}_j(\mathbf{r})$ and Ψ_j with energy $E_j = -E_i$, satisfying $\bar{\Phi}_j(\mathbf{r}) = P\bar{\Phi}_i(\mathbf{r})$ and $\Psi_j = \Psi_i^\dagger$. As a result, creating a Bogoliubov quasiparticle with energy E or removing one with energy $-E$ are indentical operations.

To see how all of this results in topological superconductivity in our wire, we start by first considering the case where $\Delta = 0$. If both $E_Z = 0$ and $\alpha = 0$, we end up with

a dispersion with a single spin degenerate parabolic band. Looking at fig 2.5(a) we see that when $\alpha \neq 0$, we end up with two parabolas that are shifted along the momentum axis, each by $k_{SO} = m\alpha$ and down in energy by $E_{SO} = m\alpha^2/2$, the spin-orbit energy, corresponding to the spin projection along the axis of the spin-orbit coupling, which in this case is the y-axis.
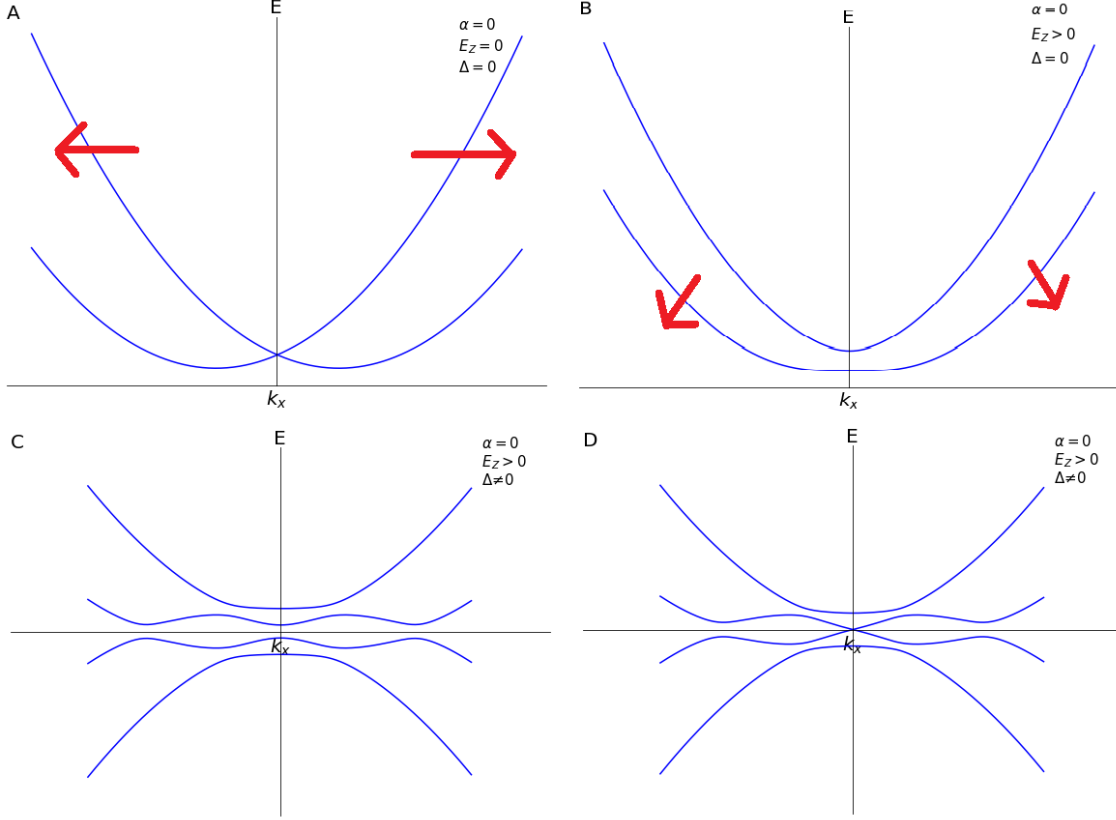
Figure 2.5: Bandstructure of a spin-orbit coupled nanowire, with magnetic field induced Zeeman splitting E_Z and superconductivity pairing term Δ. (A) The two bands are split depending on their spin polarization (red arrows). (B) The applied magnetic field, creates and energy gap between the two bands at $k_x = 0$, so there is a region without spin degeneracy, where each band holds only one spin direction, that is dependent on momentum. (C) The Δ is turned on, resulting in a doubling of the number bands. When Δ is small we have a superconducting gap associated with Majorana edge states. (D) Δ increases to the point where $E_Z = \sqrt{\Delta^2 + \mu^2}$ and the gap closes.

No spinless regime is possible here as the energy spectrum always supports an even number of Fermi points for any μ. However this changes by turning on the magnetic field so that $E_Z > 0$. The dispersion relation then becomes:

$$E_{\pm} = \frac{k_x^2}{2m} - \mu \pm \sqrt{\alpha^2 k_x^2 + E_Z^2} \tag{2.34}$$

This turns the crossing at zero momentum into an anti crossing by creating an energy gap

of size $2E_Z$, see fig 2.5(b). Because there is only one effective spin direction, placing μ within this gape makes it possible to induce "spinless" superconductivity via the proximity effect. Note that the direction of the spin depends on the momentum k_x, which is good, as the pairing term in 2.25 only couples components of the spin which are antiparallel.

We now induce superconductivity in our semiconductor, by turning on the superconducting pairing term $\Delta \neq 0$. The resulting solutions to the Bogoliubov-de Gennes equation is then:

$$E_{\pm}^2 = (\frac{k_x^2}{2m} - u)^2 + \alpha^2 k^2 + E_Z^2 + \Delta^2 \pm 2\sqrt{E_Z^2 \Delta^2 + (\frac{k_x^2}{2m} - u)^2 (E_Z^2 + \alpha^2 k_x^2)} \quad (2.35)$$

This results in a doubling of our bands, albeit without changing the number of solutions, given than positive and negative energy solutions are identical. When Δ is small we get a superconducting gap that is topological and associated with Majorana edge states, as long as the chemical potential is in the spinless regime $E_Z > \mu$, see fig 2.5(c). As Δ increases the gap at zero momentum becomes smaller, until we reach the point where $E_Z = \sqrt{\Delta^2 + \mu^2}$ at which point the gap is closed, fig 2.5(d). Increasing Δ further, reopens the gap, but now in a non-topological superconducting state. As such the criteria for topological superconductivity is:

$$E_Z > \sqrt{\Delta^2 + \mu^2} \quad (2.36)$$

To see that we have topological superconductivity when this criteria is fulfilled, we try to map the topological phase onto the spinless p-wave superconductor given in 2.2.1(a). We consider the limit $E_z \gg E_{SO}, \Delta$ and $\mu = 0$. Here the large magnetic field results in the spins in each band being nearly completely polarized, and since the energy gap is large we can ignore the higher band, and consider a single band model instead. We define $\Psi_-(x)$ as the annihilation operator for electrons at position x in lower band. As the bands are nearly spin polarized in the direction of the magnetic field, $\Psi_-(x) \approx \Psi_\downarrow(x)$, then to leading order the Hamiltonian becomes:

$$\mathcal{H}_{\text{eff}} = \int \Psi_-^\dagger(x)(\frac{k_x^2}{2m} + E_z)\Psi_-(x) + i\frac{2\alpha}{E_z}\Delta\Psi_-(x)k_x\Psi_-(x)\mathrm{d}x \quad (2.37)$$

Which is equivalent to eq 2.21(a). From the above, it is clear that as significant Zeeman splitting must necessarily be induced in the wire. This is challenging, as a large magnetic field applied across the entire setup, risk destroying the superconductivity in our s-wave superconductor. Therefore we will instead attempt to induce magnetization by creating a semiconducting wire that has both a superconducting layer and a ferromagnetic insulator layer grown onto it as suggested in [33].

2.3 Magnetism

In this section we will look at the basics of magnetic ordering and ferromagnetism in solids. As we are focusing on magnetic insulators, we will focus on material where the magnetic moments are localized and interact via exchange interaction. Most of this section is based on [39].

2.3.1 Overview of Magnetism

The magnetic moment μ is the fundamental object of magnetism. The intrinsic magnetic moment of an atom or an ion, is dependent on the total angular momentum $\mathbf{J}$ of the electrons, which itself is a sum of the orbital angular momentum $\mathbf{L}$ and the spin angular momentum $\mathbf{S}$ of the electrons:

$$\mathbf{J} = \mathbf{L} + \mathbf{S} \tag{2.38}$$

The magnetic moment of an atom or ion, and the then gives by:

$$\boldsymbol{u_J} = -g_J \mu_B \mathbf{J} \tag{2.39a}$$

2.3.2 Ferromagnetism

A ferromagnet has a spontaneous magnetization even in zero applied magnetic field. We are first going to derive a method for describing a ferromagnetic system in a similar fashion to a paramagnet in an applied magnetic field, and then we will use this model to derive some of the thermodynamic properties a ferromagnet, such a the critical temperature for spontaneous magnetiztion.

For a ferromagnet in an applied magnetic field $\mathbf{B}$ the system can be described by the Heisenberg Hamiltonian:

$$H = -\sum_{ij} \mathrm{J}_{ij} \mathbf{S}_i \cdot \mathbf{S}_j + g_J \mu_B \sum_j \mathbf{S}_i \cdot \mathbf{B} \tag{2.40}$$

Where the first term on the right is the Heisenberg exchange energy, with J_{ij} being the exchange constant between the spin on i^{th} and the spin on the jth site, which for for nearest neighbouring sites is positive for ferromagnetic alignment. The second term on the right is Zeeman energy of the external field acting on the spin at site i. Note that the term "spin" here is a bit misleading since the projection of $\mathbf{S_i}$ and $\mathbf{S_j}$ in the z-direction can take any number m_j of the total angular momentum $\mathbf{J}$. In order to make progress we make use of the mean field approximation. We assume that the interaction between the spin on site i

14

and its neighboring spins, can be described by the molecular field:

$$\mathbf{B}_{mf} = \frac{2}{g_J \mu_B} \sum_j \mathrm{J}_{ij} \mathbf{S}_j \approx \frac{2\langle \mathbf{S} \rangle}{g_J \mu_B} \sum_j \mathrm{J}_{ij} \tag{2.41}$$

Were we in the last term has replaced the spin $\mathbf{S}_j$ with its average value $\langle \mathbf{S}_J \rangle = \langle \mathbf{S} \rangle$. The exchange part of the Hamiltonian for the spin on site i can then be written as:

$$H_i = -2\mathbf{S}_i \cdot \sum_j \mathrm{J}_{ij} \mathbf{S}_j \approx -g_J \mu_B \mathbf{S}_i \cdot \mathbf{B}_{mf} \tag{2.42}$$

The total effective the effective Hamiltonian can be written as:

$$H = -g\mu_B \sum_i \mathbf{S}_i \cdot (\mathbf{B} + \mathbf{B}_{mf}) \tag{2.43}$$

which is similar to the Hamiltonian for a paramagnet in a magnetic field. Now since the magnetization of an ensemble of magnetic moments is equal to the average moment per unit volume, and the magnetic moment is related to the spin, we get:

$$\mathbf{M} = n\langle \mu \rangle = ng_J \mu_B \langle \mathbf{S} \rangle \tag{2.44}$$

were n i the number of magnetic moments per unit volume. The molecular field is then given by

$$\mathbf{B}_{mf} = \frac{2}{ng_J^2 \mu_B^2} \left(\sum_j \mathrm{J}_{ij} \right) \mathbf{M} = \lambda \mathbf{M} \tag{2.45}$$

were the constant λ parameterises the strength of the molecular field. We are now able to treat the problem as if we were dealing with paramagnet placed in a magnetic field $\mathbf{B}_{tot} = \mathbf{B} + \mathbf{B}_{mf}$. We let the external magnetic field point in the z-direction, $\mathbf{B} = B\hat{z}$, and assume that the magnetic moments and the molecular field lie in the direction of the external field. The energy of the magnetic states is then given by

$$E_{m_J} = -m_J g_J \mu_B B_{tot} \tag{2.46}$$

the partition function is then

$$Z = \sum_{m_J=-J}^{J} \exp\left(-E_{m_J}/k_B T\right) = \sum_{m_J=-J}^{J} \exp\left(m_J g_J \mu_B B_{tot}/k_B T\right) \tag{2.47}$$

setting $x = g_J \mu_B B_{tot}/k_B T$ the average value of m_J is then:

$$\langle m_J \rangle = \frac{M}{n g_J \mu_B} \frac{\sum_{m_J=-J}^{J} m_J \exp{(m_J x)}}{\sum_{m_J=-J}^{J} \exp{(m_J x)}} = \frac{1}{z} \frac{\partial Z}{\partial x} \tag{2.48}$$

This leads to the magnetization being:

$$M = n g_J \mu_B \langle m_J \rangle = \frac{n g_J \mu_B}{Z} \frac{\partial Z}{\partial B} \frac{\partial B}{\partial x} = n k_B T \frac{\partial \ln Z}{\partial B} \tag{2.49}$$

As the partition function is a geometric series it can be rewritten to

$$Z = \frac{\sinh((2J+1)\frac{x}{2})}{\sinh(\frac{x}{2})} \tag{2.50}$$

and substituting $y = xJ$ we find that

$$M = n k_B T \frac{\partial \ln Z}{\partial B} = M_s \mathrm{B}_J(y) \tag{2.51}$$

where $M_s = n g_J \mu_B J$ is the saturation magnetization, that is the maximum magnetization that can be obtained by all the magnetic moments being aligned, and $\mathrm{B}_J(y)$ is the Brillouin function:

$$\mathrm{B}_J(y) = \frac{2J+1}{2J} \coth(\frac{2J+1}{2J} y) - \frac{1}{2J} \coth(\frac{y}{2J}) \tag{2.52}$$

Which goes from -1 as $y \leftrightarrow -\infty$ to $+1$ as $y \leftrightarrow \infty$. Now if we set $B = 0 \leftrightarrow B_{tot} = B_{mf}$ the magnetization becomes:

$$M = M_s \mathrm{B}_J(\frac{g_J \mu_B J B_{mf}}{k_B T}) = M_s \mathrm{B}_J(\frac{g_J \mu_B J \lambda M}{k_B T}) \tag{2.53}$$

For low temperatures the molecular field will align the magnetic moments, but the alignment of the magnetic moments is what gives rise to the molecular field in the first place. As the temperature is raised, the thermal fluctuations of the magnetic moments causes the magnetization to progressively decrease until, and at a critical temperature T_C the magnetization is zero. This is called the Weiss model of ferromagnetism. Now due to the "chicken and egg" situation of the relationship between the molecular field and the alignment of the magnetic moments we need to solve the equations

$$\frac{M}{M_s} = \mathrm{B}_J(y) \tag{2.54a}$$

$$y = \frac{g_J \mu_B J(B + \lambda M)}{k_B T} \tag{2.54b}$$

simultaneously, this can not be solved analytically, but it can be solved numerically or graphically.
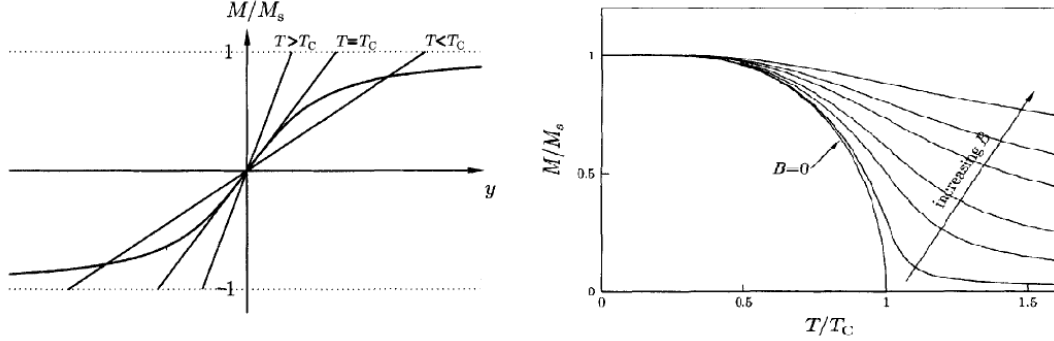
Figure 2.6: (Left) The graphical solution for 2.54a and b, at $\mathbf{B} = \mathbf{0}$. (Right) The mean field magnetization for $J = \frac{1}{2}$ as a function of temperature, caluclated at varying values of the applied field $\mathbf{B}$. Phase transition occurs only when $\mathbf{B} = 0$ [39]

We start with the case where the applied field $B = 0$, then $M = k_B T y / g_J \mu_B J \lambda$. As illustrated to the left in fig 2.6, the straight line produced by plotting M against y has a gradient which is proportional to the temperature T. By plotting the Brillouin function against we can find simultaneous solution to eqs. 2.54(a) and 2.54(b) at the points where the line and the Brillouin function intercept. For the high temperature case, the only simultaneous solution is at $y = 0$ and $M_s = 0$, and a such we have no magnetization. On the other hand, we see that at low temperatures we get three solutions, one at $M_s = 0$ and two for M_s at $\pm$ some non-zero value. It turns out that when the gradient of the line is than that of the Brillouin function at origin, the non-zero solutions are stable while the zero solution is unstable. Therefore when the system is below a critical value T_C a non-zero magnetization occurs, which grows as the material is cooled. We therefore get a magnetized material even in the absence of an external field, and it is this spontaneous magnetization which is characteristic of ferromagnetism. The transition temperature, or Curie temperature as it is also called, T_C, can be found when the gradient of the line $M = k_B T y / g_J \mu_B \lambda M_s$ and the curve $M = M_s \mathrm{B}_J(y)$ are equal at the origin. For small y the Brillouin function can be approximated to $\mathrm{B}_J(y) = (J + 1)y / 3J + O(y^3)$, an so the Curie temperature is then defined by:

$$T_C = \frac{g_J \mu_B (J + 1) \lambda M_s}{3 k_B} \tag{2.55}$$

The molecular field is then equal to:

$$B_{mf} = \lambda M_s = \frac{3 k_B T_C}{g_J \mu_B (J + 1)} \tag{2.56}$$

17

which means that for a ferromagnet with $J = \frac{1}{2}$ and $T_C \sim 10^3 K$, $B_{mf} \sim 1500T$, which is an enormous field, and reflects the strength of the exchange interactions.

So far we have assumed that the external magnetic field is zero. If we now add an external magnetic field, its effect is the that the straight line in fig 2.6 get shifted to the right, and so for all temperatures we have a non-zero magnetization thereby removing the phase transition as seen in the on the right in fig 2.6. This means that for a ferromagnet in a magnetic field, there is always an energetic advantage to line up the magnetic moments with the magnetic field, resulting in a non-zero magnetization in the same direction as the field. It is worth noting that our model assumes a completely isotropic system, which in reality is unrealistic. These anisotropies means that a real system, even without an external magnetic field will have preferred direction of its magnetization.

2.3.3   Ferromagnetic thin films

So far we have looked at the bulk properties of the magnetic material, that is deep inside of sufficiently large structures. In our case, however, we are dealing with a thin magnetic film deposited on a non-magnetic substrate, which will change some of the properties. First, while there is a constant magnetization within the film, this deviates at the surfaces, as can be seen in fig 2.7. The free surface at the top will experience and increase in magnetization due reduced coordination number which means a more atomic-like behavior is present [31]. On the other hand at the bottom, and at the top if we put a non magnetic layer on top of the ferromagnetic layer, the interface between the ferromagnetic layer and the substrate, or capping layer, result in a reduction in magnetic moments, due to the hybridization between the electronic states of the atoms of the ferromagnetic film and the interface layer.
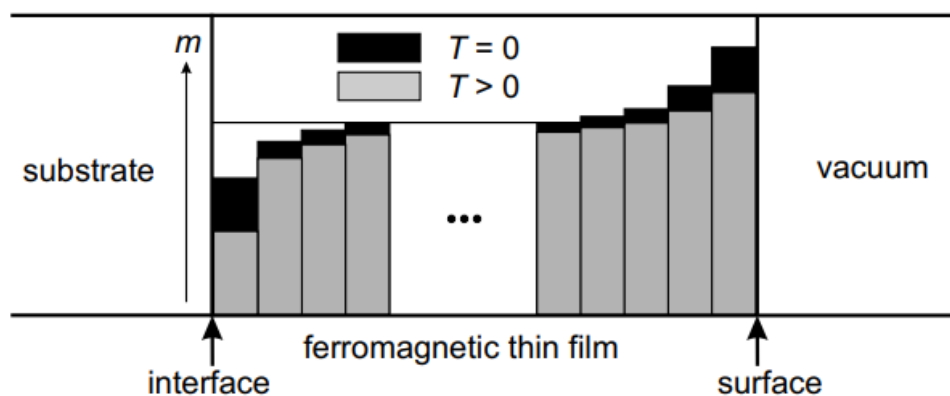
Figure 2.7: Illustration of the variation of the magnetic moment **m** per atomic layer near an interface with a substrate and near the surface at both $T = 0$ and $T > 0$ [31].

Due to the fewer neighbours on the surface spins, we get a reduction of the B_{mf}. This

reduction in magnetization doesn't just happen at the surface layer, but in several layers near the surface.

Influence by Anisotropies

A material can have many different anisotropies, all of which can typically be combined to a constant K. In a thin film, however, the broken symmetry at the interface results in the effective constant being divided in two parts, with one describing the volume contribution, and the other the surface contribution.

$$K_{\text{eff}} = K_V + \frac{2K_S}{d} \tag{2.57}$$
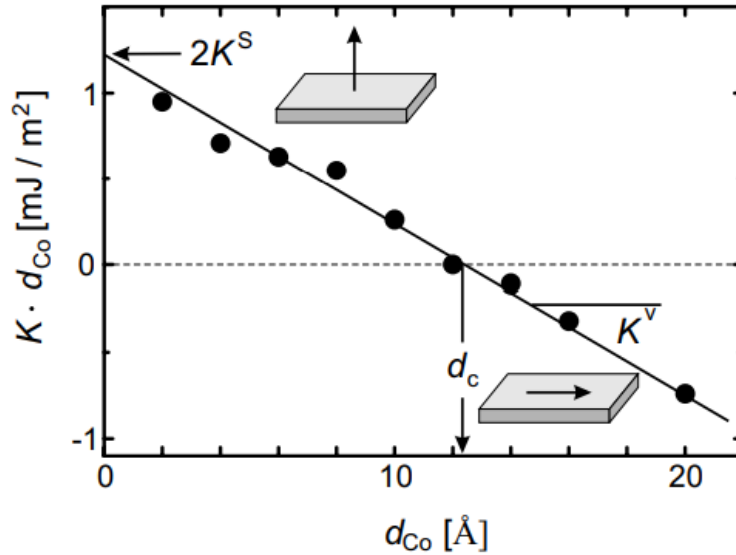
Figure 2.8: The Magnetic anisotropy in a thin film layer of Co, in a Co/Pd multilayer, as a function of the thickness d_{Co}. K_V can be determined from the slope. The zero crossing amounts to 2KS. [31]

With K_V being the volume dependent anisotropy constant and K_S being the surface dependent anisotropy constant, where the factor of two is because there are two surfaces, and d is the thickness of the magnetic system [31]. The influence of this surface anisotropy results in the so called "spin reorientation transition". As shown in figure 2.8, where the function $d \cdot K_{\text{eff}}(d) = d \cdot K_V + 2K_S$ has been plotted, K_V, which has a negative value, dominates for thick films, causing the magnetization to being in the plane of the film. However the relative amount of the surface contribution, increases as thickness d decrease, until the thickness comes below a critical value, d_c which result in a spin reorientation transition, which causes the magnetization to be perpendicular to the plane. So if we want

our thin film to be magnetized in the plane we need to apply an external magnetic field.

2.4 Coexisting superconductivity and ferromagnetism

The creation of our topological superconductor relies on two things: The induction of superconductivity in our semiconductor, and the spin splitting of the Cooper pairs, induced by a magnetic field. The penetration of the superconducting state into a normal metal, also called the proximity effect, is a well established phenomena [13, 16, 26, 37]. If a superconductor is put in contact with a normal metal (S|N), a superconducting state will arise in the in the normal metal. This state is characterised by the coherence length in the normal state (N), $\xi_N = \nu_F/2\pi T$ in the clean limit, and $\xi_N = \sqrt{D_N/2\pi T}$ in the dirty limit, where ν_F is the Fermi velocity, and D_N is the diffusion coefficient. The clean limit refers to the case where the superconducting coherence ξ_S is much smaller than the electron mean free path l, $\xi \ll l$ and the dirty limit is the case where it is much biiger $\xi \gg l$. There are different ways to describe this proximity effect. One is the Ginzburg-Landau approach and makes use of the boundary conditions at the S-N interface [16, 26], and result in the superconducting order parameter existing beyond the boundary of the superconductor, and decays into N, see fig 2.9 (a).
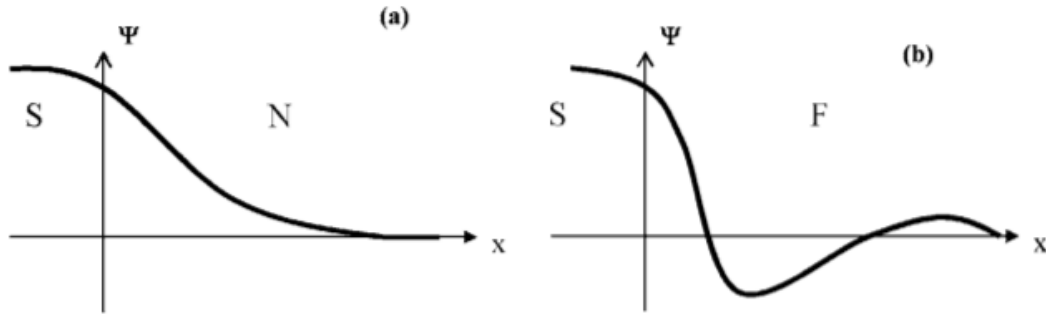
Figure 2.9: Illustration of the behavior of the superconducting order parameter at the interface between a superconductor and a normal metal and at the interface between a superconductor and a ferromagnet. [13]

Another description is the tunneling model [26, 34], where superconducting state in N comes from the Cooper pairs tunneling into the normal metal. Here it is assumed that the superconducting ordering parameter is constant, so this model assumes that the thickness of N is smaller than ξ_N.

So the problem of inducing superconductivity in our semiconductor is solved, all that remains is the spin splitting. Superconductivity and ferromagnetism are inherently antagonistic phenomena [10, 13, 20]. There are two mechanisms which causes this antagonism.

The first is related to the magnetic field, which below a critical value will be expelled by the Meissner effect, and above it suppresses the superconducting state. The second mechanism is the paramagnetic effect. An attraction between electrons creates Cooper pairs in a singlet state, whereas the exchange field of a ferromagnet wants to align the spins corresponding to a triple state. Therefore, if the Zeeman energy of a Cooper pair in the exchange field exceed the coupling energy, the superconducting state is destroyed. In the case of a pure paramagnetic effect, the critical field H_p can be found from by comparing the energy gain from spin polarization in the normal state,

$$\Delta E_N = -\chi_n \frac{H^2}{2} \tag{2.58}$$

and the superconducting condensation energy,

$$\Delta E_S = -N(0)\frac{\Delta_0^2}{2} \tag{2.59}$$

where $\chi_n = g\mu_B N(0)$ is the spin susceptibility of the normal metal, μ_B is the Bohr magneton, the g-factor is 2, $N(0)$ is the density of state at the Fermi level, and $\Delta_0 = 1.76k_B T_C$ is the superconducting gap energy at $T = 0$ [13]. Setting $\Delta E_N = \Delta E_S$ we find the paramagnetic limit at $T = 0$.

$$H_p(0) = \frac{\Delta_0}{\sqrt{2}\mu_B} \tag{2.60}$$

So as there is a region of field, below $H_p(0)$ where a coexistence of spin-splitting and superconductivity is possible.

2.4.1 SC - FMI - SM structure

Now while previous work has been done on SC-SM-FMI structures [41], and our group has previously done work on a FMI-SM structure [29], we will in this project instead test a Superconductor-Ferromagnetic Insulator-Semiconductor heterostructure, see fig 2.10, based on [33]. In this situation the ferromagnetic insulator should besides inducing a magnetization in the semiconducting layer, also act as a barrier resulting in a spin-asymmetric tunneling of electrons from the superconductor, into the semiconducting layer, thereby increasing the spin splitting field inside the semiconductor.
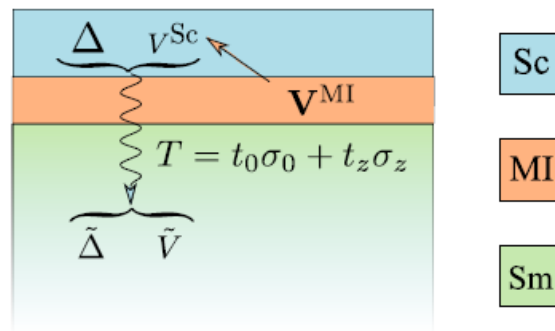
Figure 2.10: A schematic of an SC-FMI-SM hetereostructure, here the ferromagnetic insulator acts as a barrier, resulting in a spin-asymmetric tunneling of electrons from the superconductor, which should increase the spin-splitting field in the semiconductor.

3 Polarized Neutron Reflectometry

Polarized neutron reflectometry (PNR) is useful to probe the properties of materials inside a thin film of stratified media, such as the magnetization, composition and the thickness of each media. In this section we will explain how the reflection from an interface is dependent not only on the choice of media, bus also the materials below it, the thickness of the individual materials, the roughness of their interface and even any magnetization that may be present. We will also give a short explanation of how the measured result from an PNR experiment can be used to calculate these different parameters. Most of this section is based on [27] and [30], while 4.2.5 is based on [53].

3.1 Neutron basics

The neutron is an electrically neutral particle with a mass about $m_n = 1.675 \cdot 10^{-27}$kg. While electrically neutral, it still possesses a magnetic moment [27]:

$$\boldsymbol{\mu_n} = \gamma \mu_N \boldsymbol{\sigma} = \gamma \frac{e\hbar}{2m_p} \boldsymbol{\sigma} \tag{3.1}$$

where $\gamma = -1.913$ is the gyromagnetic ratio, μ_N is the nuclear magneton and $\boldsymbol{\sigma}$ is the spin state of the neutron. As we can see from γ having a negative value, the magnetic moment of the neutron couples anti parallelto its spin, which has a value of $S = 1/2$. As the neutron interacts with the nuclei via the strong nuclear force and with magnetic moments via the electromagnetic force, the reflection from a material is determined not just by the nuclei of the material, but also by its magnetism.

As a consequence of quantum mechanics, the neutron, like all other particles with a non-zero rest mass, has both particle and wave properties, and has, given a constant velocity v, a corresponding de-Broglie wavelength given by:

$$\lambda = \frac{2\pi\hbar}{mv} \tag{3.2}$$

In neutron scattering, the neutron is often described by the wave vector $\mathbf{k}$ or wave number k:

$$\mathbf{k} = \frac{m_n \mathbf{v}}{\hbar} \quad \text{and} \quad k = \frac{2\pi}{\lambda} \tag{3.3}$$

Assuming the neutrons to be non-relativistic, we can then give the kinetic energy of the neutron as:

$$E = \frac{\hbar^2 k^2}{2m_n} \tag{3.4}$$

3.2 Reflectometry

It is well known that the reflection of light from a surface is caused by the change in the refractive index at the interface. If a beam of parallel white light is sent onto the surface of a thin film, the interference between the light reflected at the top surface and the bottom surface, will cause spectral colors to appear, and one can use the reflection to measure the thickness of the film. The reflection of both X-rays and neutrons are also governed by the same laws as light, but with different refractive indices. As neutrons are scattered by nuclei, the refractive index is determined not only by the density of nuclei, but also by how strongly the neutrons scatter off the nuclei. The ability to scatter neutrons differs not just from elements to elements but also from different isotopes, and is given by the quantity called the *scattering length*, b_j. The refractive index of a material is then dependent on the scattering length density of nucleus comprising the material and the wavelength of the neutrons [15].

3.2.1 Refractive index

Using Snell's law $n_1 sin(\theta_1) = n_2 sin(\theta_2)$, we can see that the refractive index of a medium is equal to $n_m = \frac{\lambda_0}{\lambda_m} = \frac{k_m}{k_0}$, the refractive index of a neutron wave can then be found by solving the Schrödinger equation for the neutron wave motion:

$$\frac{\hbar^2}{2m_n} \frac{\mathrm{d}^2 \psi}{\mathrm{d}r^2} + (E - \overline{V})\psi = 0 \tag{3.5}$$

Where E is the total energy of the neutron and $\overline{V}$ is the spatial average of the neutron potential $V(\mathbf{r})$. A neutron propagating in a medium will experience the average scattering length of all the nuclei in the material. The potential for the interaction of a neutron with

a nucleus is given by the Fermi pseudo potential:

$$V_j(\mathbf{r}) = \frac{2\pi\hbar^2}{m_n} b_j \delta(\mathbf{r} - \mathbf{r_j}) \tag{3.6}$$

and so the average potential becomes:

$$\overline{V} = \frac{1}{volume} \int V(\mathbf{r})\,\mathrm{d}\mathbf{r} = \frac{2\pi\hbar^2}{m_n} N_b \tag{3.7}$$

where $N_b = \sum_j \dfrac{n_j b_j}{volume}$ is the scattering length density, n_j is the number of nucleui j and the b_j its scattering length.

Rewriting (3.5) in terms of the wave number k we get:

$$\frac{\hbar^2}{2m_n} \frac{\mathrm{d}^2\psi}{\mathrm{d}r^2} + k^2\psi = 0 \tag{3.8}$$

where

$$k^2 = \frac{2m}{\hbar^2}(E - \overline{V}) \tag{3.9}$$

and as the mean potential experienced by a neutron in vacuum is equal to zero, $\overline{V} = 0$, while the total energy E is conserved, we get that:

$$k_0^2 = \frac{h^2}{2m}E = (\frac{2\pi}{\lambda})^2 \tag{3.10}$$

and

$$k_m^2 = \frac{2m}{\hbar}(E - \frac{2\pi\hbar^2}{m}N_b) = \frac{2m}{\hbar}E - 4\pi N_b = k_0^2 - 4\pi N_b \tag{3.11}$$

resulting in:

$$n^2 = \frac{k_m^2}{k_0^2} = 1 - \frac{4\pi N_b}{k_0^2} = 1 - \frac{4\pi N_b}{(2\pi/\lambda_0)^2} = 1 - \frac{\lambda_0^2}{\pi}N_b \tag{3.12}$$

with the refractive index often Taylor expanded to $n \approx 1 - \frac{\lambda_0^2}{2\pi}N_b$ [27] [15].

3.2.2 Reflection from a flat interface

The potential for a wave changes at the interface between media, resulting in the wave front of the incident wave gets split up into a reflected and a transmitted, or refracted, part as illustrated in figure 3.1(a). The incident wave is described by the wavevector $\mathbf{k_i}$ and subtends an angle θ_i with the interface, while the reflected part of the wave is described by the wavevector $\mathbf{k_r}$ and subtends an angle θ_r. In the case we are looking at the incident angle equals the reflected angle $\theta_i = \theta_r$ and the momentum transfer is normal to the
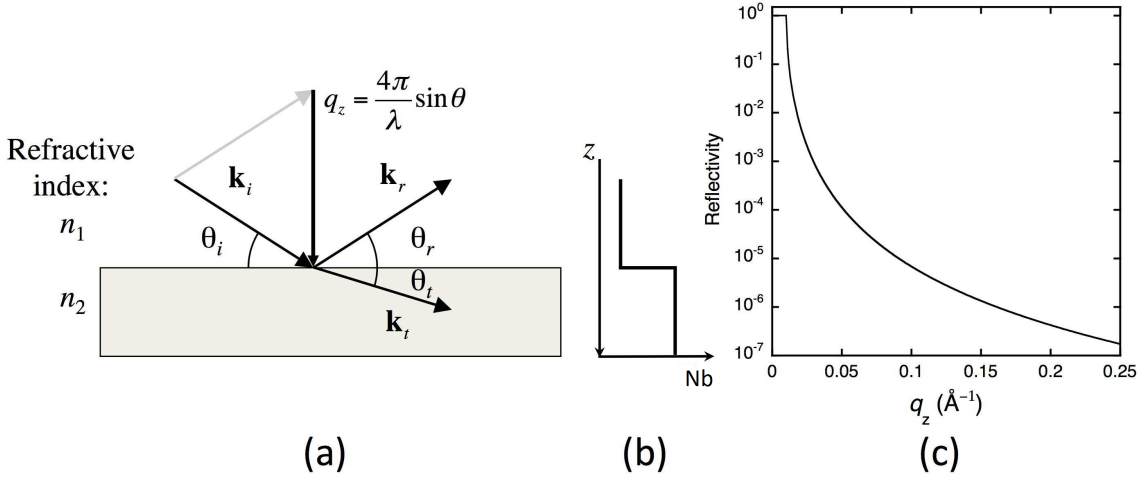
Figure 3.1: Schematics of (a) an incident neutron wave $\mathbf{k_1}$ being split into a reflected $\mathbf{k_r}$ and a refracted $\mathbf{k_t}$ wave at the interface between to media. (b) Graph of the scattering length density along the normal to the surface. (c) Calculated specular neutron reflectivity as function of the momentum transfer vector $\mathbf{q} = \mathbf{k_r} - \mathbf{k_i}$, for an air/silicon interface. [27]

interface, also called specular scattering. Furthermore part of the wave can be transmitted with the angle θ_t and wavevector $\mathbf{k_t}$. As the wave only changes in the direction normal to the surface, the z direction, the problem becomes one dimensional. As such we plot the scattering length density as a function of the depth, z, in the sample, as seen in figure 3.1(b).

In order to find the reflection and the transmission of the neutron beam, we solve the Schrödinger equation for each medium [30].

$$\frac{\hbar^2}{2m}\nabla^2\psi_1 + (E - V_1) = 0 \tag{3.13a}$$

$$\frac{\hbar^2}{2m}\nabla^2\psi_2 + (E - V_2) = 0 \tag{3.13b}$$

Which have the solutions:

$$\psi_1 = \psi_i^0 e^{-i(k_x x + k_y y + k_{i,z} z)} + \psi_r^0 e^{-i(k_x x + k_y y - k_{i,z} z)} \tag{3.14a}$$

$$\psi_2 = \psi_t^0 e^{-i(k_x x + k_y y + k_{t,z} z)} \tag{3.14b}$$

Note that $k_{r,z} = -k_{i,z}$, and that k_x and k_y is the same for both the incident, reflected and transmitted wave. As the boundary condition we have continuity of both the wave $\psi_1 = \psi_2$ and of its derivative $\frac{d\psi_1}{dz} = \frac{d\psi_2}{dz}$ at the interface, $z = 0$, resulting in;

$$\psi_i^0 + \psi_r^0 = \psi_t^0 \tag{3.15a}$$

26

$$- k_{i,z}\psi_i^0 + k_{i,z}\psi_r^0 = -k_{t,z}\psi_t^0 \tag{3.15b}$$

Solving these two equations we get:

$$\psi_r^0 = \frac{k_{i,z} - k_{t,z}}{k_{i,z} + k_{t,z}}\psi_i^0 = r\psi_i^0 \tag{3.16a}$$

$$\psi_t^0 = \frac{2k_{i,z}}{k_{i,z} + k_{t,z}}\psi_i^0 = t\psi_i^0 \tag{3.16b}$$

With r and t being the Fresnel coefficients for respectively reflection and transmission. In an experiment when we measure the reflectivity, what we measure is the intensity of the incoming neutron beam versus the reflected beam, and so the reflectivity is defined as:

$$R(q_z) = \frac{I_r(q_z)}{I_i} = \frac{|\psi_r^0|^2}{|\psi_i^0|^2} = |r|^2 \tag{3.17}$$

Where instead of giving the reflectivity as a function of the angle, we have defined it as a function of the wave vector transfer $q_z = \frac{4\pi \sin(\theta_i)}{\lambda} = 2k_z$, and so $|r|^2 = |\frac{q_{i,z}-q_{t,z}}{q_{i,z}+q_{t,z}}|^2$. A simulation of the reflectivity for an air/silicon interface as function of q_z is can be seen in figure 3.1(c). As one can see the figure shows a small range where there is total reflection i.e. $R(q_z) = 1$. Rewriting eq. 3.11 in terms of q_z we get:

$$q_{i,z} = \sqrt{q_{0,z}^2 - 16\pi N_{b1}} \tag{3.18a}$$

$$q_{t,z} = \sqrt{q_{0,z}^2 - 16\pi N_{b2}} = \sqrt{q_{i,z}^2 - 16\pi(N_{b2} - N_{b1})} \tag{3.18b}$$

From this we see that when $q_{i,z}^2 \leq 16\pi(N_{b2} - N_{b1})$, then $q_{t,z}$ is imaginary and then $r = 1$ resulting in total reflection. The critical edge is defined as the largest q where $r = 1$:

$$q_c = \sqrt{16\pi(N_{b2} - N_{b1})} \tag{3.19}$$

And so the reflectivity can be written as [15]:

$$R = |r|^2 = \left| \frac{q_{i,z} - (q_{i,z}^2 - q_c^2)^{1/2}}{q_{i,z} + (q_{i,z}^2 - q_c^2)^{1/2}} \right|^2 \tag{3.20}$$

3.2.3 Reflection from a stratified media

So far we have only looked at reflection from a single layered interface. On the other hand if we have a stratified media, a material with numerous layers of thin films like the one we are examining, there are multiple interfaces in our medium, which end up affecting the
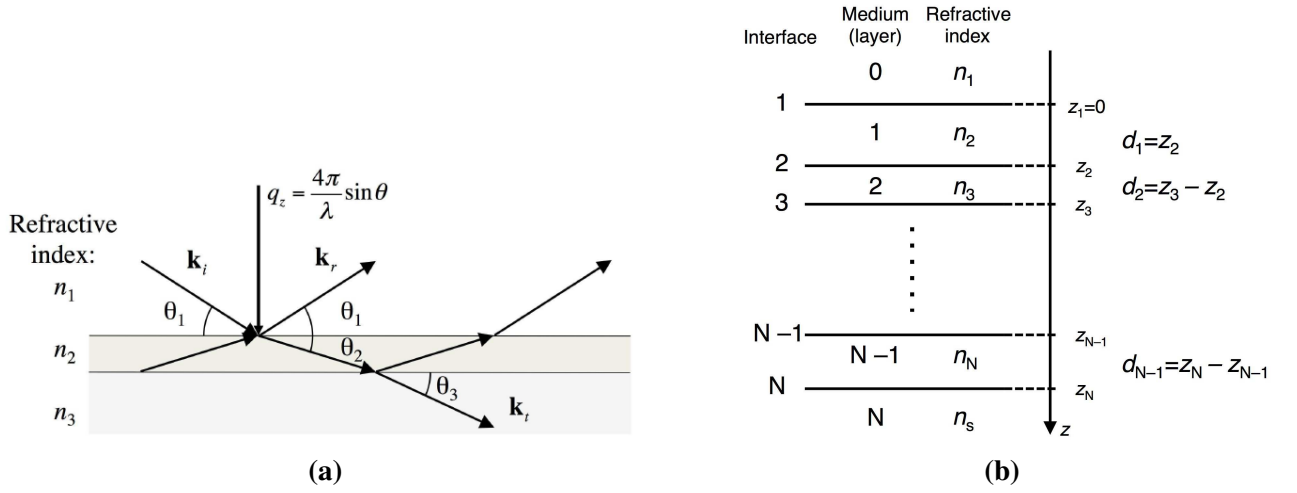
Figure 3.2: Reflection from a multilayered sample. (a) The schematics of the four waves interacting at an interface. (b) The numbering system of a multilayered sample. [27]

overall reflection. Looking at figures 3.2 (a), we see that besides the reflected wave, the refracted wave and the incident wave from above the interface, an additional wave from below the surface must also be taken into account. This second wave, is the reflected wave from the layers deeper in the surface, so it is only at the interface deepest in the sample that the second incident wave don't need to be considered. The phase and amplitude of this second incident wave is modified by the path length through film and so it depends on the thickness d of the film, resulting in the amplitude of the wave being modified by the factor:

$$a_j = e^{-2ik_{jz}d_j} = e^{-iq_{jz}d_j} \tag{3.21}$$

The waves reflected at different interface in the sample, will interfere with one another, causing fringes in the reflection, as seen in figure 3.3(a), with the number of fringes increases with d. In order to get the actual reflection from our sample, we then need to sum up the reflection from each layer in the sample. This can be done in two ways, here we focus on what is called the recursive method. We number our sample similar to figure 3.2(b), so that the reflection for interface j is described as the reflection between medium $j-1$ and j, and the waves have same number as their medium. The reflection from the last interface N is simply the Fresnel coefficient multiplied by the amplitude factor:

$$r_{N-1,N} = \frac{k_{N-1,z} - k_{N,z}}{k_{N-1,z} + k_{N,z}} e^{-2ik_{N-1}d_{N-1}} = f_{N-1,N} a_{N-1} \tag{3.22}$$

28

The reflected wave is then included in the calculation of the reflection from the next interface $j = N - 1$, through a recursion formula:

$$r_{j-1,j} = \frac{f_{j-1,j} + f_{j,j+1} a_j}{1 + f_{j-1,j} f_{j,j+1} a_j} \qquad (3.23)$$

This recursion is then performed all the way up to the top layer $r_{0,1}$, which then gives us the total reflection:

$$R = |r_{0,1}|^2 \qquad (3.24)$$

This is know as the Parrott formalism.

(a)   **(b)**
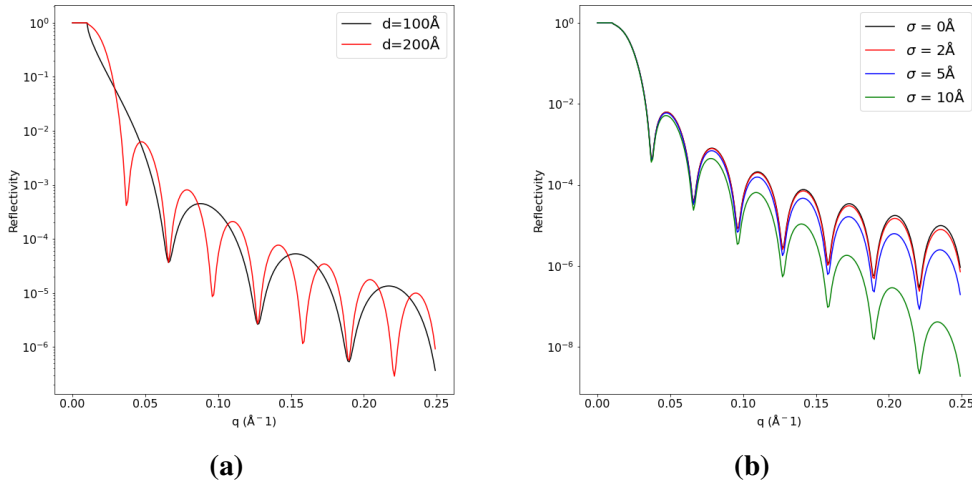
Figure 3.3: Reflection from multilayered sample calculated in python. (a) The calculated reflection from two samples, consisting of a film of iron (Fe), on silicon (Si), with different thickness of Fe. Note that the 200 Å sample has two minima for every one of the 100 Å. The distance between the fringes is $\frac{2Pi}{d}$ (b) Calculated reflection from 200 Å Fe/Si sample, with different values of roughness. Note the effect of the roughness becomes bigger as q_z increases.

3.2.4   Reflection from a rough interface

So far we have assumed that the reflection happens from perfect interfaces. Unfortunately interfaces are never perfect, and in reality our scattering length density will not take the form of a step function like in figure 3.1(b). Instead it will be more continuous either due to grading across the interface or roughness of the interface, something which we can not distinguish between with specular reflection. In order to take account for the roughness and grading of the interface, we use make use of a method devised by Croce and Névot [36]. A model for the sample is constructed like before, but now we assume that each interface have a Gaussian profile in z. Applying a Fourier transformation over

the interface, then modifies the Fresnel coefficient to:

$$f_{j-1,j} = \frac{k_{j-1,z} - k_{j,z}}{k_{j-1,z} - k_{j,z}} e^{-2k_{j_1}k_j\sigma_j^2} \tag{3.25}$$

Where σ_j is the width of the Gaussian profile for the jth interface. This equation can be substituted directly with the Fresnel equation as previously given. As can be seen in figure 3.3(b) the roughness decrease the reflectivity, with larger decrease as q_z increases.

3.2.5 Reflection from a magnetic interface
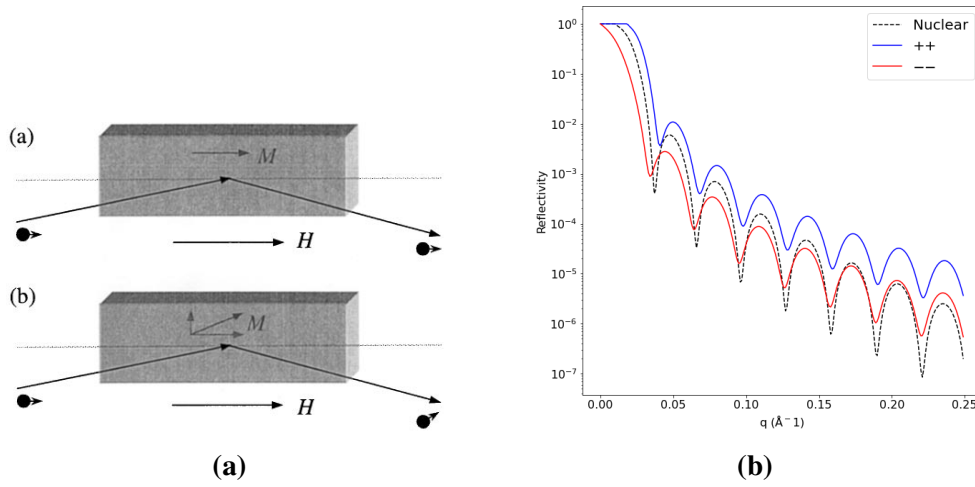
Figure 3.4: Reflection from a magnetic material. (a) The orientation of the magnetization **M** of the sample, relative to the applied field **H**, determines the proportion of spin-flip and non spin-flip scattering [21]. (b) The reflection from a magnetic material with magnetization and applied field parallel to the surface.

So far we have assumed that the only interaction between the neutrons and the reflective material is the nuclear interaction. However, as the neutron possesses a spin and a resulting intrinsic magnetic moment, its reflection may also depend on the orientation of the spin. This is for instance the case when the neutron scatters off a magnetic material. The addition of the magnetization changes the potential experienced by the neutron so it becomes:

$$V = V_n + V_m = V_n \mp \underline{\mu}\mathbf{B} \tag{3.26}$$

Where $\mathbf{B} = \mu_0\mathbf{M}$ is magnetic induction vector and $\underline{\mu} = \mu_n\underline{\sigma}$ is the magnetic moment of the neutron, with $\underline{\sigma}$ being a linear combination of the Pauli matrices, and $\mu_n = -1.913\mu_N$. In a PNR experiment an external **B** field will be applied and it is that which we define the polarization of the neutron along. In our experiment the B-field is applied parallel to the surface of our sample, similar to figure 3.4(a), so we have the neutron polarized in

the x-direction, and the depth of our sample in the z-direction. The $\mp$ in equation 3.26 is negative (positive) if the spin of the neutron is parallel (anti-parallel) to the applied field, and so the value $-\mu_n B$ is positive, resulting in an increased potential. However, if the magnetization has a component that is not parallel to the applied field, as in figure 3.4(ab), then it is possible for the neutron to undergo a spin-flip, so for example an incident neutron with a positive spin gets reflected with a negative spin. Writing equation 3.26 in matrix form we get,

$$V = V_n \mp \mu_n \begin{vmatrix} B_x & B_z - iB_y \\ B_z + iB_y & -B_x \end{vmatrix} \tag{3.27}$$

where we assume that positive values of B, are from spins parallel to the field. For simplicity, we define a magnetic scattering length density $\boldsymbol{\rho_m}$ similar to the neutron scattering length density [53]:

$$\boldsymbol{\rho_m} = C \sum_i^J N_i \boldsymbol{\mu_i} = -\frac{m_n}{2\pi\hbar^2} \mu_n \mu_0 \sum_i^J \mathbf{M_i} \tag{3.28}$$

Where for the magnetic moment per formula unit $\boldsymbol{\mu}$, expressed in units of μ_B, $C = 2.645 \cdot 10^{-5} \text{Å} \mu_B^{-1}$. We then write the potential in terms of the scattering length density:

$$V = \frac{2\pi\hbar^2}{m_n} \begin{vmatrix} N_b + \rho_{m,x} & \rho_{m,z} - i\rho_{m,y} \\ \rho_{m,z} + i\rho_{m,y} & N_b - \rho_{m,x} \end{vmatrix} \tag{3.29}$$

Taking into account the spin dependence of the neutron and the spin dependence of the scattering potential, the solution to the Schrödinger equtation becomes:

$$\psi = U_+ \begin{vmatrix} 1 \\ 0 \end{vmatrix} e^{ik_{+,z}z} + U_- \begin{vmatrix} 0 \\ 1 \end{vmatrix} e^{ik_{-,z}z} \tag{3.30}$$

Where $|U_+|^2 + |U_-|^2 = 1$, the vectors are the orientation of the spin and $k_{\pm,z}$ is the z component of the wavevector for the different neutron spin state, which as previously mentioned sees a change in the potential depending on its orientation:

$$k_\pm = \sqrt{k_0^2 - 4\pi(N_b \pm |\boldsymbol{\rho_m}|)} \tag{3.31}$$

Which means that the magnetic material in effect is birefringent. In our experiment we assume that the magnetization of our material is parallel to the applied field, so the off-diagonal values in (3.29) are zero. Two measurements of the reflectivity are then performed, one for spin-up $U_+ = 1, U_- = 0$ neutrons, and one for spin-down $U_+ = 0, U_- = 1$. Comparing the reflectivity for spin-up R^{++} with the one for spin-down R^{--} and the nuclear reflectivity, one can calculate the strength and depth profile of the

magnetization in the sample. A theoretical calculation of a Fe/Si sample can be seen in figure 3.4(b), as can be seen the reflection of spin-up neutron is bigger than the just the nuclear reflection, while the reflection from the spin-down is smaller. It should of course be remembered that the reflection at an interface is determined by the difference in potential energy, of the the two media making up the interface, therefore it is possible to have situation where neutron in the spin-down state, has a bigger reflection. Besides normal spin-up and spin-down reflection, where we merely measure the reflectivity of a neutron with a given spin, it is also possible to have situation where there is a spin-flip, so for example an incoming neutron with spin-up hits the surface, and get flip to a spin-down state. This spin-flip though is only induced by the components of the B-field, which are perpendicular to the surface.

3.3 Analysis

Once we have conducted a PNR experiment, we need to analyse the data. This is done using the computer program GenX [11]. In the program we create a starting model of our sample, that is the we write the materials, with their scattering length density and their the approximate thickness. The data sets from each of our measurements is then loaded in to the program. For a PNR experiment, that means we have at least two reflection curves, one for spin-up and one for down. The program simulates the theoretical reflection from the given start values of our sample, and afterwards it can be used to fit the thickness of each layer, the size of the magnetization and the roughness of the interfaces.

4 Instruments

In this chapter the instruments that have been used in our polarized neutron reflectometry experiments will be presented.

4.1 D17

D17 is a neutron reflectometer located at the Institut Laue-Langevin (ILL) in France [1], where the neutron are provided by a high flux reactor, so we have a countinous neutron source. D17 has a horizontal scattering geometry (vertical surfaces). At the sample position, the white neutron beam flux is $6.9 \cdot 10^9 \text{n} \cdot \text{s}^{-1} \cdot \text{cm}^{-2}$, which combined with the low instrumental background allows one to measure reflectivities down to 10^{-7}. D17 can operate in four modes, time of flight (TOF) (bottom of fig 4.1), monochromatic (top of fig 4.1) and polarized versions of the these two modes. In our experiment we use the polarized TOF mode. In the TOF mode a double chopper system with a variable phase is used to transmit a neutron beam with a wavelength in the range of 2 to 30Å, and wavelength dependent resolution of 0.5-20% (FWHM). The beam is then polarized, by moving a supermirror S-bender into its path, see bottom fig 4.1, resulting in a large section of the neutrons in the wavelength band from 4 to 20Å becoming polarized. The S-bender is made of a stack Si wafers measuring $50\text{mm(length)} \times 160\text{mm(height)} \times 200\mu\text{m(thick)}$, which are coated with an inverted $m = 3.2$ Fe/Si supermirror and 600nm thick Gd absorption layer. These waifers are bent into a symmetric S shape with a radius of curvature of 10m. This S-bender is placed in a permanent magnet assembly, which provides a vertical field strength of 500G at the exit of the device. The direction of polarization of the neutron, both before and after the sample, can be manipulated with the adiabatic radio frequency spin flippers (RF) [40]. In case of specular scattering the polarization analysis is performed by a $m = 3.2$ Fe/Si supermirror coating on a 1cm thick absorbing borofloat substrate in reflection geometry. At the sample position, the sample is placed in a crymoagnet, used for cooling and applying a small magnetic field. The measurable q range is $0.002\text{Å}^{-1} < q < 2\text{Å}^{-1}$. The specifications can be seen in table 4.1. The m value mentioned for the Fe/Si multilayer, is the relation between the

critical scattering vector q_c of a multilayer, and the critical scattering vector of Nickel $q_{c,\text{Ni}} = 0.0217\text{Å}^{-1}$ [27]. So the critical scattering vector for the Fe/Si multilayer is:

$$q_c = m q_{c,\text{Ni}} \tag{4.1a}$$

$$q_{c,\text{Fe/Si}} = 3.2 \cdot 0.0217\text{Å}^{-1} = 0.06944\text{Å}^{-1} \tag{4.1b}$$

D17 Specifications	
Mode	Polarized TOF
Chopper spin rate	550 - 3000 rpm
Chopper separation	75mm
Chopper phase	0-20 deg
Incident wavelength	4-20Å
q range	$0.002\text{Å}^{-1} < q < 2\text{Å}^{-1}$
Resolution	0.5-20% (FWHM)
Polarizer	Fe/Si multilayer S-bender
Polarisation analysis	Polarizing Fe/Si mirror analyzer.
White beam flux	$9.6 \cdot 10^9 \text{n} \cdot \text{s}^{-1} \cdot \text{cm}^{-2}$
Beam area at sample	6×50mm (width $\times$ height)

Table 4.1: Table of specifications for D17, relevant for the performed experiment. Values are taken from [1].

4.2 POLREF

POLREF is a neutron reflectometer located at ISIS in England [2]. The neutrons are provided via spallation, so it is a pulsed neutron source. Like D17 it uses time of flight to determine the wavelength band of the neutrons. The specifications can be seen in table 4.2, and an outline can be seen in fig 4.2.

POLREF Specifications	
Mode	Polarized TOF
Incident Wavelength	0.9 - 15Å
Resolution	3-10% (FWHM)
White beam flux	$\sim 10^7 \text{n} \cdot \text{s}^{-1} \cdot \text{cm}^{-2}$
Beam area at sample	60×30mm (H $\times$ V)

Table 4.2: Table of specifications for POLREF, relevant for the performed experiment. Values are taken from [22].
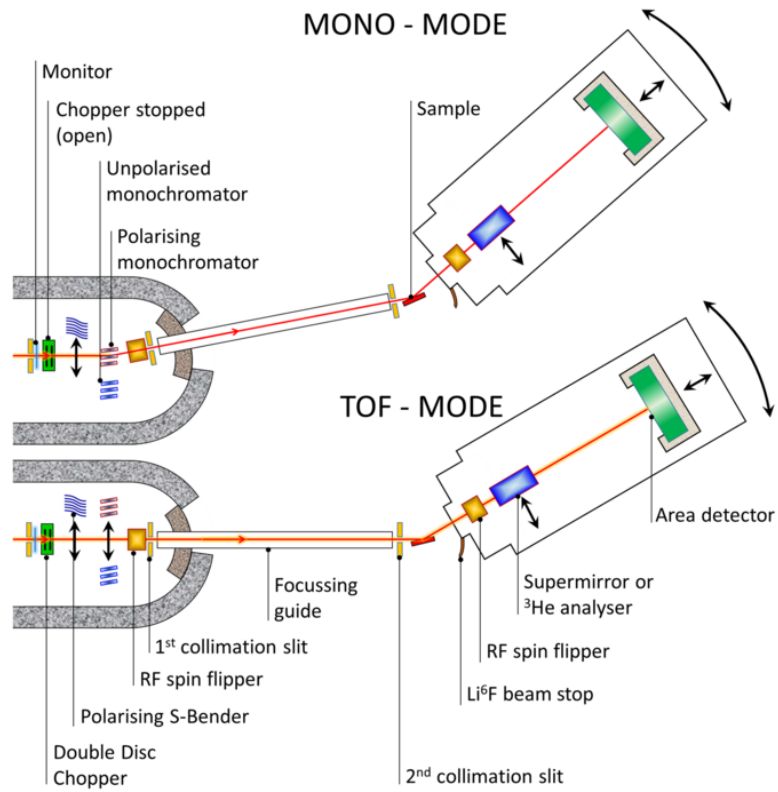
Figure 4.1: Schematic of D17, taken from [1]. We are using the TOF mode.
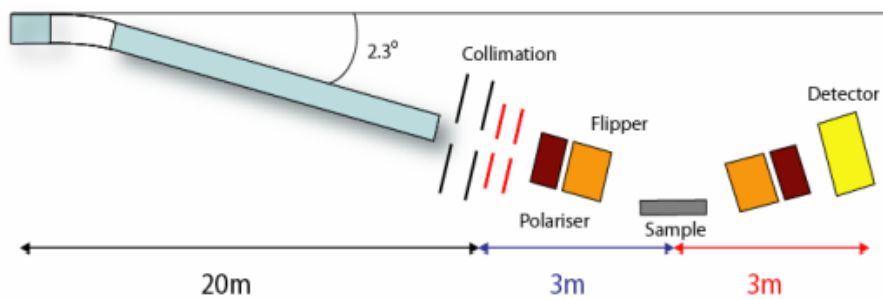
Figure 4.2: Outline of POLREF, taken from [22].

5 Samples

In this section we will give a description of the two samples on which we have performed our experiments. The samples have been created by Y. Liu at University of Copenhagen. We have two samples: Qdev1001 and Qdev1002. Both samples are about $20\text{mm} \times 20\text{nm}$ and consist of a substrate of indium arsenide (InAs), a semiconductor, then a layer of europium sulfide (EuS), a ferromagnetic insulator with $T_c = 16.5\text{K}$, and at saturation it has a magnetic moment per formula unit of $m = \frac{6.9\mu_B}{(5.969\text{Å})^3}$ [39], then a layer of lead (Pb), a bulk type 1 superconductor with $T_s = 7.2\text{K}$, a penetration depth of $\lambda = 87\text{nm}$, a coherence length of $\xi = 39\text{nm}$ and a critical field of $H_c = 803.4\text{Oe}$ [6, 14], and then a layer of Al_2O_3, which is a cap layer which is there to protect the sample from oxidization and environmental impurities. A schematic of the samples can be seen in 5.1a. The initial size of the layers was obtained using high-resolution transmission electron microscopy (HRTEM), an example of which can be seen in fig 5.1b.

(a)

(b)
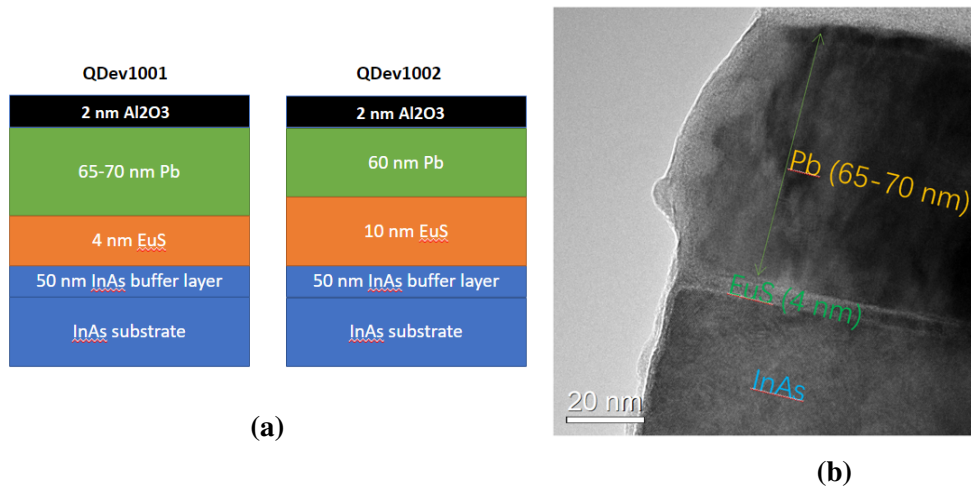
Figure 5.1: (Left) A schematic representation of the the samples Qdev1001 and Qdev1002, the thickness of each layers is based on HRTEM measurements. (Right) A HRTEM image of Qdev1001.

5.1 Crystal structure and scattering lenght denisty

It is important that we know the scattering length densities (SLD) of the different materials, for our PNR experiment. While the SLD for Al_2O_3 is taken from [53], the rest has been calculated using the crystal structure [?, 25], and the scattering length for the different nuclei [43]. The results are shown in table 5.1.

	Al_2O_3	Pb	EuS	InAs
Structure		FCC	Cubic rock salt ($Fm3\overline{m}$)	Zinc blende ($F\overline{4}3m$)
Lattice parameter [Å]		4.95	5.969	6.048
SLD [$\times 10^{-6}$Å^{-2}]	5.21	3.10	1.893	1.925

Table 5.1: Crystal structure, and scattering length densities for materials in the samples.

6 Results

In this section we will present the data that have been gathered from our polarized neutron reflectometry experiments on and the two samples. Furthermore, we will also present the results of our data fits.

6.1   Qdev1001

The experiment on the sample Qdev1001 was conducted on D17, at ILL, by M. Tripathi and K. Dalal from the University of Copenhagen, and T. Saerbeck, first responsible on D17. Using time of flight, the instrument sent out of a beam of polarized neutrons with a wavelength in the range $\lambda = 2$-27Å, which at the sample position have a beam area of 20mm $\times$ 6mm.

The sample was mounted on a holder, see fig 6.1, pre-aligned at room temperature, and then cooled to 2K in a cryomagnet, at 0T. Once a temperature of 2K had been reached, the alignment was checked and the measurements could start. The measurement was done in a 0.1T applied magnetic field, aligned with the polarization of the neutrons, in the x-axis, so the field lies with the surface. This was is done to ensure an alignment of all the magnetic moments in the europium sulfide layer, are in the same direction.

Figure 6.1: The sample Qdev1001, mounted in a holder.

Measurements on the sample were done at two beamtimes, the first starting on 11/08/2020 and the second starting on 4/08/2021. At the first beamtime measurements were taken at temperatures of 2K, 8K, 12K 20K, 50K and 300K all at 0.1T. On the second, measurements were taken at 2K and 8K, in order to ensure that the sample were not degraded. Then

measurements were taken 6K and 7K. Measurements were also taken for at an applied field of 0.25T and 1T, both at 2K. The data are plotted in fig. 6.2
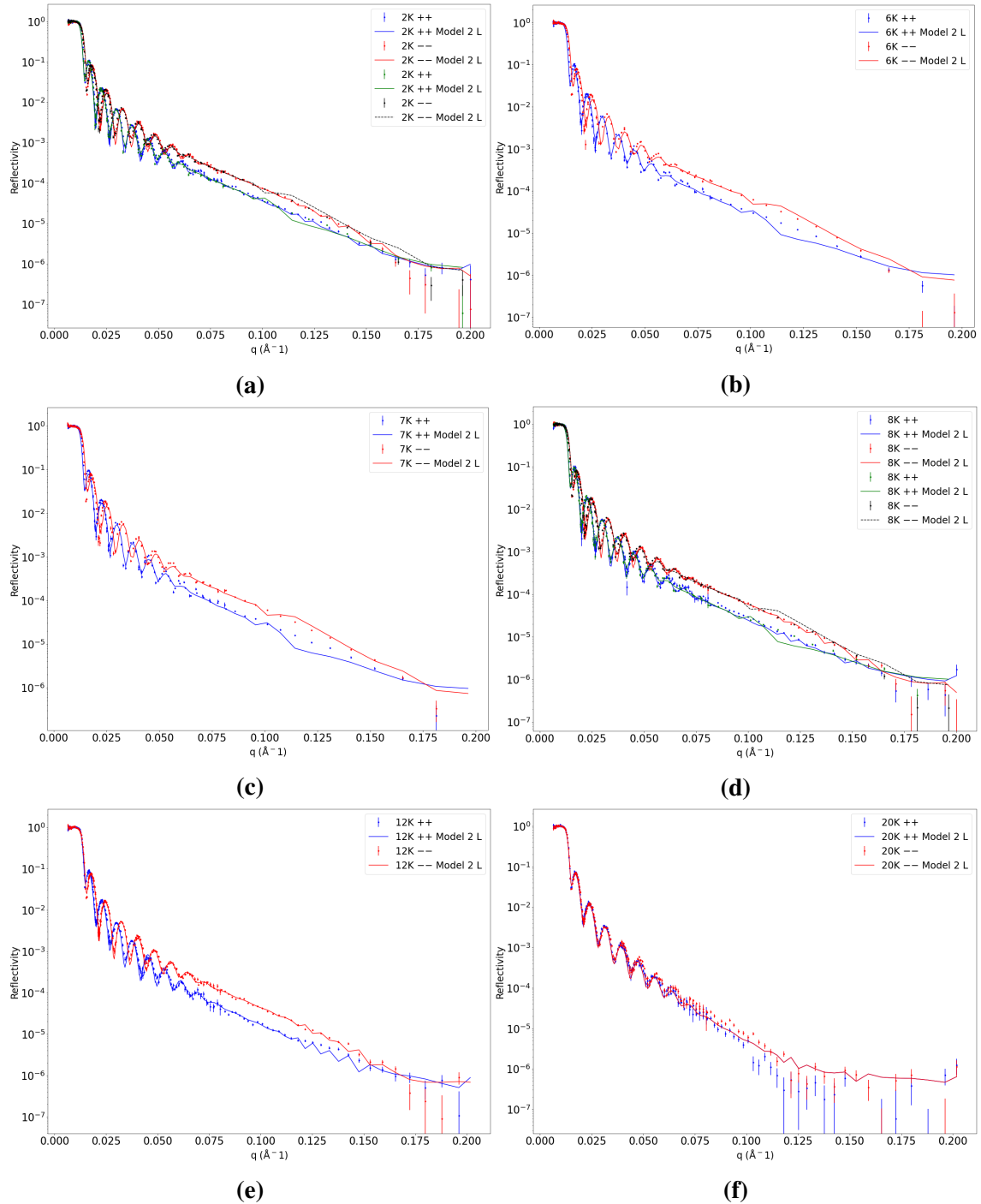
Figure 6.2

Looking at the plots of the data, fig 6.2, we can clearly see that for temperatures from less than 16K, (6.2a-6.2e) the reflection of neutrons with a spin-down polarization R^{--} is
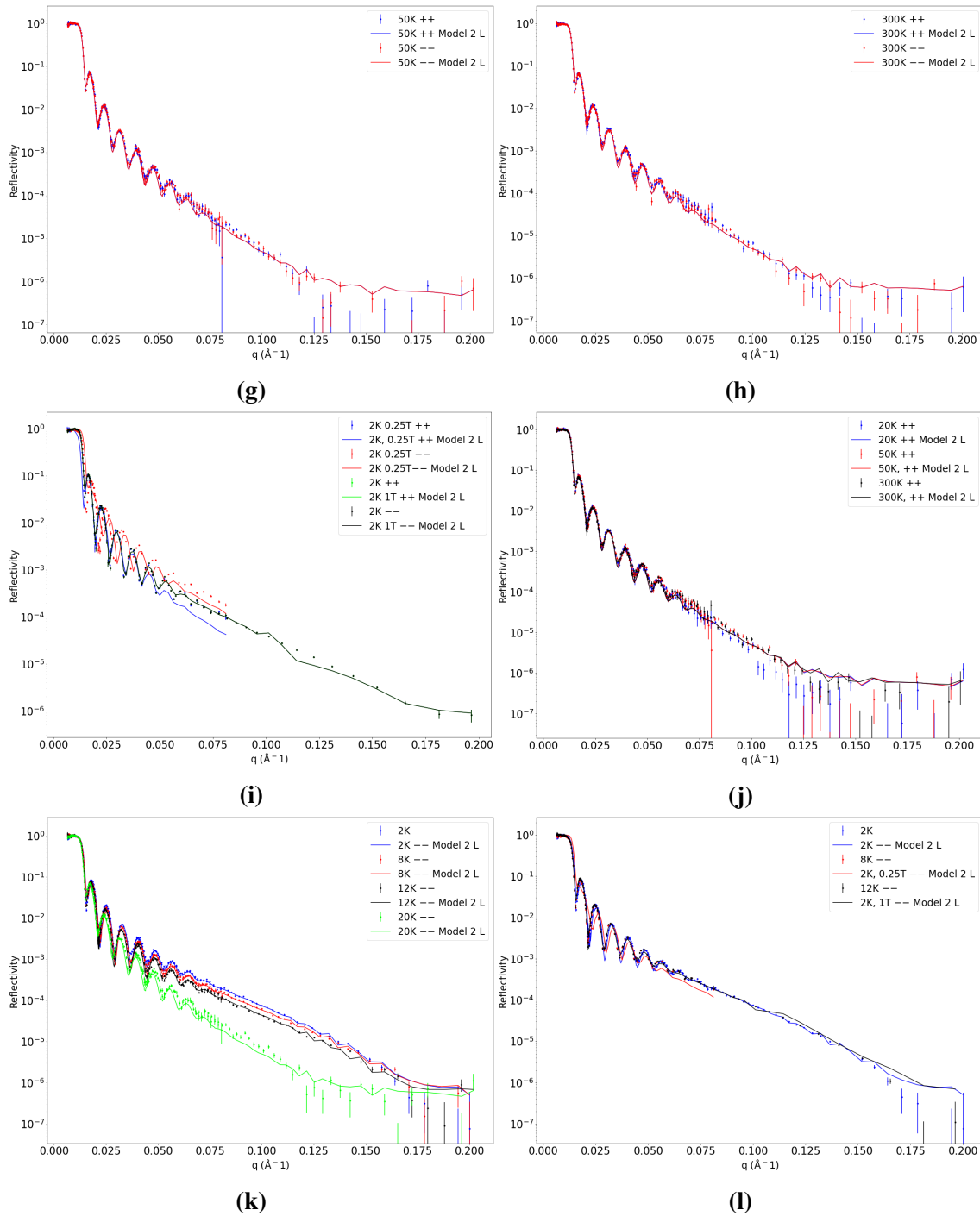
Figure 6.2: Plots of the data form the PNR experiment conducted on Qdev1001. Plot a-h shows the reflection for different temperatures with an applied field of $B = 0.1\text{T}$, while i-l compares different magnetization and different temperatures. The simulated profile of the long range version of model 2, as described later, is also plotted.

stronger than the reflection of neutrons with a spin-up polarization R^{++}. At the same time we see that for temperatures above 16K (6.2f-6.2h) the reflection is the same for both spin orientation, but also for for all three temperatures 6.2j. This is fitting with the presence

of ferromagnetism, below the Curie temperature of EuS. Comparing data from above and below the Curie temperature, $T_C = 16.5K$, fig 6.2k, we can see a significant change in the reflection, between the ferromagnetic, and the paramagnetic state. We can also see minor difference between the reflection for $T = 12K$, where we are in the ferromagnetic regime of EuS, but above T_c for Pb, and the reflection for $T = 8K$ were we are near T_c, and $T = 2K$ where we are below T_c.

6.1.1 Models and simulations

In order to determine the structure of the sample the we will be using fitting the data with GenX. By creating a model of the sample, the program simulates the theoretical reflection and compares it to the given data. By letting the program run, it can then fit the different parameters of the sample to the data, in order to determine the structure. Now as it is a simulation, the program uses a model of the instrument, see fig 6.3, which we have to set based on the instrument used for the experiment. In this case we set the wavelength of the neutrons to $\lambda = 5\text{Å}$, and uses polarized neutrons as a probe.
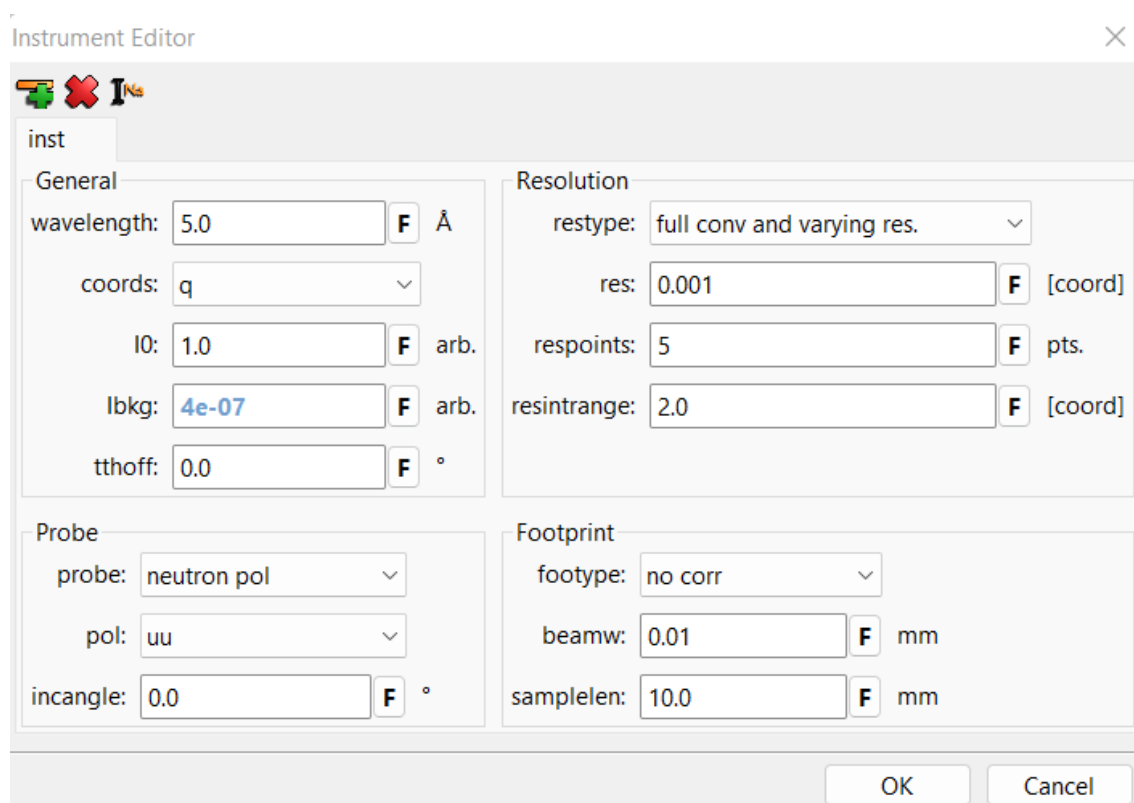
Figure 6.3: The instrument setting for Qdev1001.

We start by first fitting the structure of the sample, using a χ^2 fit, from our data taken at 20K, 50K and 300K, where we determine the thickness d of the layers and the roughness

σ of the interfaces. Furthermore, due to the Al_2O_3 layer being very thin, and not perfect, but in fact may consist of island deposits, we also fit the scattering length b for Al_2O_3. The results can be seen in table 6.1.

Structure ($\chi^2 = 4.7262$)		
Parameter	Values	Error
$\sigma_{Al_2O_3}[\mathring{A}]$	12.14	$(-8.417 \cdot 10^{-7}, 0.1998)$
$d_{Al_2O_3}[\mathring{A}]$	18.68	$(-7.069 \cdot 10^{-7}, 0.1999)$
$b_{Al_2O_3}[fm]$	9.912	$(-0.09994, 7.719 \cdot 10^{-6})$
$\sigma_{Pb}[\mathring{A}]$	2.00	$(-1.438 \cdot 10^{-6}, 4.505)$
$d_{Pb}[\mathring{A}]$	736.00	$(-3.345, 3.090)$
$\sigma_{EuS}[\mathring{A}]$	4.6924	$(-2.248, 2.848)$
$d_{EuS}[\mathring{A}]$	33.915	$(-5.514, 5.172)$
$\sigma_{InAs}[\mathring{A}]$	2.00	$(-1.854 \cdot 10^{-5}, 4.999)$

Table 6.1: The structure values of Qdev1001. Note that this is only fitted from the data taken at 20K, 50K and 300K. Note that the error values are the lower and upper values of the errorbars. The large differences in the values, for example σ_{Pb} where the errors are $(-1.438 \cdot 10^{-6}, 4.505)$ arises when the fitted parameter has a value very close to either the lower or upper boundaries of the fit, in this case it is close to the lower boundary

Keeping these values constant, we now fit 4 different models. In the first model, model 1, we assume that there is only a temperature dependent magnetism in the EuS layer, and that apart from the superconducting screening field in Pb, that the rest of the layers are non-magnetic, see far left fig 6.4. The result of this fit can be seen in table 6.2. Now despite the critical field for lead being $T_c \approx 0.8mT$ we assume that due to the small size of the layer, we can treat it as a type II superconductor, and that therefore superconductivity is not broken by the applied field, for values of $B = 0.1T$ and $B = 0.25T$, and it will first get broken at $B = 1T$. Unlike other parameters, the superconducting screening fields are calculated by hand, $M_{Pb,0.1T} = -0.26[\mu_B/\mathring{F}U]$, $M_{Pb,0.25T} = -0.651[\mu_B/\mathring{F}U]$, and applied as constant parameters in the fit.

Based on what we have learned in our theory, and what we are hoping to achieve, the next 3 models are fitted with the assumption of magnetism, outside EuS. In model 2, middle left fig. 6.4, we assume that some of the magnetism in EuS leaks into InAs and creates a layer of magnetization in the top of InAs, and in model 3, middle right fig. 6.4, we assume there is magnetism leaking into Pb, thereby creating a small layer of magnetization in the bottom of Pb. In the fourth model, far right fig.6.4, we assume that magnetism leaks into both InAs and Pb. Now again, as we have seen in our theory, it is possible, that if there is a magnetic proximity effect, that it is either long range, where the induced magnetization will go far into the other layers, or short range, where the induced magnetization will only be present in the first few unit cells. As such we have made two fit for each model. One
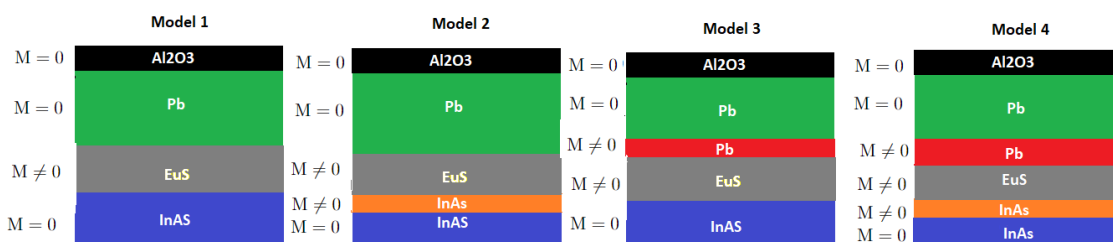
Figure 6.4: The different models that we test. (Far left) In model 1 we assume there is only magnetization in the EuS layer. (Middle left) In model 2 we assume a magnetization in both the EuS layer and some that leaks in to the top of the InAs layer. (Middle right) in model 3 assume that besides the magnetization in EuS, some leaks into bottom of the Pb layer. (Far right) in model assume that magnetization leaks into botht InAs layer and the Pb layer. Note that while $M = 0$ for lead, there is stil a small screening field, which have been taken into account.

where we set no upper limit on the thickness of the magnetic layers, and one where we assume that the magnetic layers is at maximum 5 unit cells thick. The result can be seen in table 6.3, 6.4 and 6.5

Model 1 ($\chi^2 = 50.095$)		
Parameter	Values	Errors
$\sigma_{M,EuS}[\text{Å}]$ 2K	1.5182	$(-3.139, 1.310)$
$\sigma_{M,EuS}[\text{Å}]$ 2K, 0.25T	-3.0000	$(-4.135 \cdot 10^{-7}, 9.999)$
$\sigma_{M,EuS}[\text{Å}]$ 2K, 1T	0.97797	$(-3.645, 4.033)$
$\sigma_{M,EuS}[\text{Å}]$ 6K	0.22799	$(-3.105, 4.416)$
$\sigma_{M,EuS}[\text{Å}]$ 7K	-0.48620	$(-2.478, 4.849)$
$\sigma_{M,EuS}[\text{Å}]$ 8K	$-9.4503 \cdot 10^{-3}$	$(-2.922, 2.417)$
$\sigma_{M,EuS}[\text{Å}]$ 12K	0.70184	$(-3.693, 4.957)$
$M_{EuS}[\mu_B/\text{FU}]$ 2K	5.9613	$(-0.5605, 0.6026)$
$M_{EuS}[\mu_B/\text{FU}]$ 2K, 0.25T	3.0000	$(-5.495 \cdot 10^{-9}, 2.393)$
$M_{EuS}[\mu_B/\text{FU}]$ 2K, 1T	6.4451	$(-0.6144, 0.6659)$
$M_{EuS}[\mu_B/\text{FU}]$ 6	5.1224	$(-0.3737, -0.3784)$
$M_{EuS}[\mu_B/\text{FU}]$ 7K	4.8291	$(-0.7557, 0.7613)$
$M_{EuS}[\mu_B/\text{FU}]$ 8K	4.7978	$(-0.5176, 0.4982)$
$M_{EuS}[\mu_B/\text{FU}]$ 12K	4.2905	$(-0.7509, 0.5996)$
$\sigma_{M,InAs}[\text{Å}]$ 2K	-2.0000	$(-0.9925, 8.389)$
$\sigma_{M,InAs}[\text{Å}]$ 2K 0.25T	-1.9992	$(-0.9940, 8.821)$
$\sigma_{M,InAs}[\text{Å}]$ 2K 1T	2.7960	$(-2.994, 3.037)$
$\sigma_{M,InAs}[\text{Å}]$ 6K	-1.9995	$(-0.9933, 8.435)$
$\sigma_{M,InAs}[\text{Å}]$ 7K	-2.0002	$(-0.9979, 8.754)$
$\sigma_{M,InAs}[\text{Å}]$ 8K	-1.9997	$(-0.9917, 8.639)$

$\sigma_{\mathrm{M,InAs}}[\text{Å}]$ 12K	-2.0025	$(-0.9967, 8.958)$

Table 6.2: The fitted parameter values for model 1 for Qdev1001.

Model 2				
	Long Range ($\chi^2 = 37.936$)		Short Range ($\chi^2 = 41.206$)	
Parameter	Values	Errors	Values	Errors
$\sigma_{\mathrm{M,EuS}}[\text{Å}]$ 2K	0.94807	$(-0.7717, 0.7278)$	2.2987	$(-1.516, 0.6997)$
$\sigma_{\mathrm{M,EuS}}[\text{Å}]$ 2K, 0.25T	-2.0000	$(-4.178 \cdot 10^{-7}, 6.999)$	-2.0000	$(-1.933 \cdot 10^{-5}, 4.999)$
$\sigma_{\mathrm{M,EuS}}[\text{Å}]$ 2K, 1T	1.5820	$(-0.8246, 1.118)$	-0.37526	$(-1.049, 1.025)$
$\sigma_{\mathrm{M,EuS}}[\text{Å}]$ 6K	0.49505	$(-0.9839, 0.9255)$	2.1537	$(-3.997, 0.5497)$
$\sigma_{\mathrm{M,EuS}}[\text{Å}]$ 7K	-1.6554	$(-0.9381, 0.6991)$	2.0170	$(-0.8708, 0.9469)$
$\sigma_{\mathrm{M,EuS}}[\text{Å}]$ 8K	0.29440	$(-0.8784, 1.206)$	2.3146	$(-3.832, 0.6705)$
$\sigma_{\mathrm{M,EuS}}[\text{Å}]$ 12K	0.65300	$(-0.7842, 1.175)$	0.51828	$(-1.223, 1.126)$
$M_{\mathrm{EuS}}[\mu_{\mathrm{B}}/\text{FU}]$ 2K	5.4122	$(-0.2852, 0.2553)$	6.1072	$(-0.2752, 0.3167)$
$M_{\mathrm{EuS}}[\mu_{\mathrm{B}}/\text{FU}]$ 2K, 0.25T	3.0000	$(-3.534 \dot 10^{-8}, 1.491)$	3.0000	$(-1.251 \cdot 10^{-7}, 2.706)$
$M_{\mathrm{EuS}}[\mu_{\mathrm{B}}/\text{FU}]$ 2K, 1T	6.7889	$(-0.5496, 0.5661)$	6.3455	$(-0.5127, 0.4317)$
$M_{\mathrm{EuS}}[\mu_{\mathrm{B}}/\text{FU}]$ 6	4.5334	$(-0.3864, 0.5984)$	5.1014	$(-0.5412, 0.5967)$
$M_{\mathrm{EuS}}[\mu_{\mathrm{B}}/\text{FU}]$ 7K	4.2367	$(-0.2268, 0.7376)$	4.7607	$(-0.3725, 0.3795)$
$M_{\mathrm{EuS}}[\mu_{\mathrm{B}}/\text{FU}]$ 8K	4.0844	$(-0.08225, 0.7667)$	4.7721	$(-0.5369, 0.4696)$
$M_{\mathrm{EuS}}[\mu_{\mathrm{B}}/\text{FU}]$ 12K	4.3453	$(-0.3116, 0.5368)$	4.2983	$(-0.2393, 0.2416)$
$\sigma_{\mathrm{M,InAs}}[\text{Å}]$ 2K	1.8076	$(-0.9562, 1.404)$	3.7710	$(-5.682, 0.2286)$
$\sigma_{\mathrm{M,InAs}}[\text{Å}]$ 2K 0.25T	10.000	$(-12.00, 4.338 \cdot 10^{-6})$	-1.9955	$(-4.533 \cdot 10^{-3}, 8.994)$
$\sigma_{\mathrm{M,InAs}}[\text{Å}]$ 2K 1T	-0.054187	$(-1.754, 6.010)$	-2.0085	$(-0.9860, 8.959)$
$\sigma_{\mathrm{M,InAs}}[\text{Å}]$ 6K	-1.9982	$(-1.792 \cdot 10^{-3}, 11.99)$	2.6393	$(-2.700, 1.732)$
$\sigma_{\mathrm{M,InAs}}[\text{Å}]$ 7K	-1.9996	$(-4.096 \cdot 10^{-4}, 11.99)$	2.3013	$(-1.124, 1.427)$
$\sigma_{\mathrm{M,InAs}}[\text{Å}]$ 8K	-1.9995	$(-5.196 \cdot 10^{-4}, 9.269)$	3.3651	$(-1.622, 1.939)$
$\sigma_{\mathrm{M,InAs}}[\text{Å}]$ 12K	-1.9812	$(-0.01877, 11.98)$	-1.9952	$(-7.730, 6.207 \cdot 10^{-7})$
$d_{\mathrm{M,InAs}}[\text{Å}]$	85.842	$(-26.63, 16.72)$	25.000	$(-4.576, 4.458)$
$M_{\mathrm{InAs}}[\mu_{\mathrm{B}}/\text{FU}]$ 2K	-1.3178	$(-0.6100, 0.5307)$	-0.74364	$(-0.7025, 0.9328)$
$M_{\mathrm{InAs}}[\mu_{\mathrm{B}}/\text{FU}]$ 2K, 0.25T	-3.8473	$(-0.4354, 0.7054)$	-5.0000	$(-1.822 \cdot 10^{-7}, 2.840)$
$M_{\mathrm{InAs}}[\mu_{\mathrm{B}}/\text{FU}]$ 2K, 1T	0.99328	$(-0.8202, 0.6578)$	0.54222	$(-0.7959, 1.190)$
$M_{\mathrm{InAs}}[\mu_{\mathrm{B}}/\text{FU}]$ 6	-1.2800	$(-0.8868, 0.9440)$	-0.94733	$(-0.7907, 0.6997e)$
$M_{\mathrm{InAs}}[\mu_{\mathrm{B}}/\text{FU}]$ 7K	-1.3090	$(-0.6265, 0.6625)$	-1.0382	$(-0.9372, 1.204)$
$M_{\mathrm{InAs}}[\mu_{\mathrm{B}}/\text{FU}]$ 8K	-1.5473	$(-0.7626, 0.5578)$	-1.1242	$(-0.7346, 0.7813)$
$M_{\mathrm{InAs}}[\mu_{\mathrm{B}}/\text{FU}]$ 12K	0.12692	$(-0.7726, 0.9397)$	0.051548	$(-1.244, 1.526)$
$\sigma_{\mathrm{M,InAs-Sub}}[\text{Å}]$ 2K	57.000	$(-6.563, 7.042)$	2.4999	$(-4.996, 5.437 \cdot 10^{-5})$
$\sigma_{\mathrm{M,InAs-Sub}}[\text{Å}]$ 2K 0.25T	51.630	$(-8.574, 8.122)$	2.5000	$(-5.000, 1.558 \cdot 10^{-5})$

$\sigma_{\text{M,InAs}-\text{Sub}}[\text{Å}]$ 2K 1T	70.000	$(-69.99, 1.431 \cdot 10^{-5})$	2.5000	$(-4.999, 2.831 \cdot 10^{-5})$
$\sigma_{\text{M,InAs}-\text{Sub}}[\text{Å}]$ 6K	54.787	$(-10.26, 9.294)$	2.5000	$(-5.000, 3.953 \cdot 10^{-5})$
$\sigma_{\text{M,InAs}-\text{Sub}}[\text{Å}]$ 7K	56.721	$(-43.11e, 13.26)$	-2.4999	$(-8.064 \cdot 10^{-5}, 5.000)$
$\sigma_{\text{M,InAs}-\text{Sub}}[\text{Å}]$ 8K	56.641	$(-22.97, 10.91)$	-2.5000	$(-1.207 \cdot 10^{-5}, 5.000)$
$\sigma_{\text{M,InAs}-\text{Sub}}[\text{Å}]$ 12K	58.477	$(-6.039, 6.368)$	2.4977	$(-4.995, 2.308 \cdot 10^{-3})$

Table 6.3: The fitted parameter values for model 2 for Qdev1001.

Model 3				
	Long Range ($\chi^2 = 51.276$)		Short Range ($\chi^2 = 52.095$)	
Parameter	Values	Errors	Values	Errors
$\sigma_{\text{M,Pb}}[\text{Å}]$ 2K	4.9999	$(-4.999, 8.103 \cdot 10^{-5})$	2.5000	$(-4.499, 1.667 \cdot 10^{-5})$
$\sigma_{\text{M,Pb}}[\text{Å}]$2K, 0.25T	0.0050263	$(-5.012 \cdot 10^{-3}, 4.993)$	0.0034472	$(-1.964, 2.486)$
$\sigma_{\text{M,Pb}}[\text{Å}]$2K, 1T	0.012415	$(-1.238 \cdot 10^{-2}, 4.986)$	0.0031064	$(-1.977, 2.477)$
$\sigma_{\text{M,Pb}}[\text{Å}]$ 6K	0.013854	$(-1.385 \cdot 10^{-2}, 4.985)$	2.5000	$(-4.493, 8.856 \cdot 10^{-6})$
$\sigma_{\text{M,Pb}}[\text{Å}]$ 7K	0.0048816	$(-4.879 \cdot 10^{-3}, 4.995)$	2.5000	$(-4.499, 2.714 \cdot 10^{-6})$
$\sigma_{\text{M,Pb}}[\text{Å}]$ 8K	5.0000	$(-4.995, 5.499 \cdot 10^{-3})$	2.5000	$(-4.499, 9.517 \cdot 10^{-6})$
$\sigma_{\text{M,Pb}}[\text{Å}]$ 12K	0.018642	$(-1.862 \cdot 10^{-2}, 4.981)$	0.0053161	$(-2.005, 2.493)$
$d_{\text{M,Pb}}[\text{Å}]$	24.658	$(-3.986, 3.828)$	21.000	$(-5.151, 5.203 \cdot 10^{-8})$
$M_{\text{Pb}}[\mu_{\text{B}}/\text{FU}]$ 2K	-1.2690	$(-7.758 \cdot 10^{-2}, 0.6536)$	-1.0316	$(-0.3318, 0.6016)$
$M_{\text{Pb}}[\mu_{\text{B}}/\text{FU}]$ 2K, 0.25T	-4.0000	$(-1.276 \cdot 10^{-6}, 2.071)$	-4.0000	$(-4.158 \cdot 10^{-8}, 2.327)$
$M_{\text{Pb}}[\mu_{\text{B}}/\text{FU}]$ 2K, 1T	-1.1707	$(-0.3738, 0.9635)$	-1.2912	$(-0.2368, 0.6270)$
$M_{\text{Pb}}[\mu_{\text{B}}/\text{FU}]$ 6	-2.4873	$(-0.4384, 1.026)$	-2.0696	$(-0.2494, 0.9741)$
$M_{\text{Pb}}[\mu_{\text{B}}/\text{FU}]$ 7K	-2.5230	$(-0.4104, 0.9298)$	-2.1727	$(-0.1595, 1.003)$
$M_{\text{Pb}}[\mu_{\text{B}}/\text{FU}]$ 8K	-1.4883	$(-0.2567, 0.9127)$	-1.2751	$(-0.7507, 0.6565)$
$M_{\text{Pb}}[\mu_{\text{B}}/\text{FU}]$ 12K	-0.32224	$(-0.3053, 0.7211)$	-0.29907	$(-0.5671, 0.9338)$
$\sigma_{\text{M,EuS}}[\text{Å}]$ 2K	9.4585	$(-4.186, 0.4993)$	7.0000	$(-3.356, 1.461 \cdot 10^{-6})$
$\sigma_{\text{M,EuS}}[\text{Å}]$2K, 0.25T	7.2959	$(-9.276, 2.684)$	3.4264	$(-5.419, 3.538)$
$\sigma_{\text{M,EuS}}[\text{Å}]$2K, 1T	10.000	$(-4.545, 1.461 \cdot 10^{-5})$	7.0000	$(-4.186, 3.312 \cdot 10^{-6})$
$\sigma_{\text{M,EuS}}[\text{Å}]$ 6K	8.5333	$(-2.340, 1.316)$	7.0000	$(-4.042, 1.817 \cdot 10^{-6})$
$\sigma_{\text{M,EuS}}[\text{Å}]$ 7K	6.999	$(-3.463, 1.620)$	7.0000	$(-4.652, 6.325 \cdot 10^{-7})$
$\sigma_{\text{M,EuS}}[\text{Å}]$ 8K	9.7252	$(-4.453, 0.2748)$	7.0000	$(-4.956, 3.356 \cdot 10^{-7})$
$\sigma_{\text{M,EuS}}[\text{Å}]$ 12K	8.2336	$(-4.524, 1.638)$	7.0000	$(-8.482, 1.088 \cdot 10^{-6})$
$M_{\text{EuS}}[\mu_{\text{B}}/\text{FU}]$ 2K	6.9274	$(-0.8601, 7.839 \cdot 10^{-2})$	6.6413	$(-0.6251, 0.3318)$
$M_{\text{EuS}}[\mu_{\text{B}}/\text{FU}]$ 2K, 0.25T	3.0000	$(-4.183 \cdot 10^{-7}, 2.727)$	3.0000	$(-1.016 \cdot 10^{-7}, 2.360)$
$M_{\text{EuS}}[\mu_{\text{B}}/\text{FU}]$ 2K, 1T	7.6894	$(-1.017, 5.269 \cdot 10^{-2})$	7.5624	$(-0.6468, 0.4120)$
$M_{\text{EuS}}[\mu_{\text{B}}/\text{FU}]$ 6	5.8386	$(-1.344, 0.5158)$	5.7932	$(-0.8411, 0.1934)$
$M_{\text{EuS}}[\mu_{\text{B}}/\text{FU}]$ 7K	5.3153	$(-0.7719, 1.010)$	5.3523	$(-1.121, 0.3170)$

$M_{\mathrm{EuS}}[\mu_{\mathrm{B}}/\mathrm{FU}]$ 8K	5.4854	$(-0.8354, 5.627 \cdot 10^{-2})$	5.2551	$(-0.7428, 0.4625)$
$M_{\mathrm{EuS}}[\mu_{\mathrm{B}}/\mathrm{FU}]$ 12K	4.9086	$(-1.163, 0.6350)$	4.7846	$(-0.8526, 0.3509)$
$\sigma_{\mathrm{M,InAs}}[\mathrm{\mathring{A}}]$ 2K	0.83432	$(-2.524, 3.271)$	1.6031	$(-3.592, 3.971)$
$\sigma_{\mathrm{M,InAs}}[\mathrm{\mathring{A}}]$ 2K 0.25T	-1.9954	$(-4.615 \cdot 10^{-3}, 11.99)$	1.9955	$(-4.465 \cdot 10^{-3}, 8.992)$
$\sigma_{\mathrm{M,InAs}}[\mathrm{\mathring{A}}]$ 2K 1T	3.9313	$(-1.378, 2.346)$	7.0000	$(-8.997, 1.854 \cdot 10^{-6})$
$\sigma_{\mathrm{M,InAs}}[\mathrm{\mathring{A}}]$ 6K	10.000	$(-11.99, 7.517 \cdot 10^{-6})$	7.0000	$(-9.000, 4.132 \cdot 10^{-6})$
$\sigma_{\mathrm{M,InAs}}[\mathrm{\mathring{A}}]$ 7K	10.000	$(-12.00, 1.8300 \cdot 10^{-5})$	7.0000	$(-8.985, 2.636 \cdot 10^{-6})$
$\sigma_{\mathrm{M,InAs}}[\mathrm{\mathring{A}}]$ 8K	-1.9797	$(-2.031 \cdot 10^{-2}, 10.910)$	1.0809	$(-0.8808, 3.422)$
$\sigma_{\mathrm{M,InAs}}[\mathrm{\mathring{A}}]$ 12K	-1.9984	$(-1.628 \cdot 10^{-6}, 11.99)$	1.9984	$(-1.623 \cdot 10^{-3}, 8.960)$

Table 6.4: The fitted parameter values for model 3 for Qdev1001.

Model 4				
	Long Range ($\chi^2 = 37.838$)		Short Range ($\chi^2 = 47.483$)	
Parameter	Values	Errors	Values	Errors
$\sigma_{\mathrm{M,Pb}}[\mathrm{\mathring{A}}]$ 2K	9.9999	$(-9.999, 1.611 \cdot 10^{-7})$	0.0021	$(-2.116 \cdot 10^{-3}, 2.498)$
$\sigma_{\mathrm{M,Pb}}[\mathrm{\mathring{A}}]$ 2K, 0.25T	9.9999	$(-10.00, 1.938 \cdot 10^{-6})$	2.4999	$(-2.500, 2.349 \cdot 10^{-6})$
$\sigma_{\mathrm{M,Pb}}[\mathrm{\mathring{A}}]$ 2K, 1T	0.0070	$(-7.097 \cdot 10^{-3}, 9.990)$	2.4999	$(-2.500, 5.676 \cdot 10^{-4})$
$\sigma_{\mathrm{M,Pb}}[\mathrm{\mathring{A}}]$ 6K	0.0367	$(-3.667 \cdot 10^{-2}, 9.962)$	0.01422	$(-1.418 \cdot 10^{-2}, 2.481)$
$\sigma_{\mathrm{M,Pb}}[\mathrm{\mathring{A}}]$ 7K	0.0083	$(-8.328 \cdot 10^{-3}, 9.970)$	0.0133	$(-1.337 \cdot 10^{-2}, 2.486)$
$\sigma_{\mathrm{M,Pb}}[\mathrm{\mathring{A}}]$ 8K	0.0020	$(-2.062 \cdot 10^{-3}, 9.993)$	0.0040	$(-4.036 \cdot 10^{-3}, 2.494)$
$\sigma_{\mathrm{M,Pb}}[\mathrm{\mathring{A}}]$ 12K	0.0183	$(-1.838 \cdot 10^{-2}, 9.973)$	0.0066	$(-6.663 \cdot 10^{-3}, 2.493)$
$d_{\mathrm{M,Pb}}[\mathrm{\mathring{A}}]$	25.3562	$(-4.849, 0.1212)$	15.9168	$(-3.498, 5.060)$
$M_{\mathrm{Pb}}[\mu_{\mathrm{B}}/\mathrm{FU}]$ 2K	-1.2115	$(-0.1744, 0.3940)$	-0.7201	$(-0.7615, 0.1197)$
$M_{\mathrm{Pb}}[\mu_{\mathrm{B}}/\mathrm{FU}]$ 2K, 0.25T	-3.999	$(-4.488 \cdot 10^{-8}, 1.811)$	-1.5507	$(-2.437, 0.3578)$
$M_{\mathrm{Pb}}[\mu_{\mathrm{B}}/\mathrm{FU}]$ 2K, 1T	-0.6302	$(-0.5148, 0.4123)$	-2.6733	$(-0.4593, 1.411)$
$M_{\mathrm{Pb}}[\mu_{\mathrm{B}}/\mathrm{FU}]$ 6	-2.1410	$(-0.4538, 0.4299)$	-1.4899	$(-0.3032, 1.080)$
$M_{\mathrm{Pb}}[\mu_{\mathrm{B}}/\mathrm{FU}]$ 7K	-2.1983	$(-0.3316, 0.4462)$	-1.4440	$(-0.3365, 1.549)$
$M_{\mathrm{Pb}}[\mu_{\mathrm{B}}/\mathrm{FU}]$ 8K	-1.9582	$(-0.2247, 0.2817)$	-0.5005	$(-0.6628, 0.5381)$
$M_{\mathrm{Pb}}[\mu_{\mathrm{B}}/\mathrm{FU}]$ 12K	-0.2146	$(-0.2520, 0.3438)$	-0.2598	$(-0.9850, 0.8367)$
$\sigma_{\mathrm{M,EuS}}[\mathrm{\mathring{A}}]$ 2K	6.9999	$(-2.944, 1.394 \cdot 10^{-6})$	8.2477	$(-2.381, 1.734)$
$\sigma_{\mathrm{M,EuS}}[\mathrm{\mathring{A}}]$ 2K, 0.25T	4.4424	$(-1.637, 3.356 \cdot 10^{-3})$	-1.9999	$(-7.323 \cdot 10^{-6}, 12.00)$
$\sigma_{\mathrm{M,EuS}}[\mathrm{\mathring{A}}]$ 2K, 1T	6.9999	$(-4.168, 1.519 \cdot 10^{-6})$	8.4789	$(-2.197, 1.519)$
$\sigma_{\mathrm{M,EuS}}[\mathrm{\mathring{A}}]$ 6K	6.9999	$(-4.386, 3.164 \cdot 10^{-6})$	7.8492	$(-3.051, 0.6739)$
$\sigma_{\mathrm{M,EuS}}[\mathrm{\mathring{A}}]$ 7K	6.9999	$(-4.264e, 2.625 \cdot 10^{-6})$	7.5265	$(-3.524, 1.791)$
$\sigma_{\mathrm{M,EuS}}[\mathrm{\mathring{A}}]$ 8K	6.9999	$(-3.753, 1.595 \cdot 10^{-6})$	7.7834	$(-1.106, 1.205)$
$\sigma_{\mathrm{M,EuS}}[\mathrm{\mathring{A}}]$ 12K	6.9999	$(-8.980, 5.312 \cdot 10^{-9})$	7.9233	$(-4.602, 1.993)$
$M_{\mathrm{EuS}}[\mu_{\mathrm{B}}/\mathrm{FU}]$ 2K	5.8070	$(-0.1701, 0.5321)$	6.8701	$(-5.684 \cdot 10^{-2}, 1.196)$

$M_{\text{EuS}}[\mu_{\text{B}}/\text{FU}]$ 2K, 0.25T	3.0000	$(-2.524 \cdot 10^{-6}, 2.049)$	3.0000	$(-3.031 \cdot 10^{-6}, 2.749)$
$M_{\text{EuS}}[\mu_{\text{B}}/\text{FU}]$ 2K, 1T	7.3141	$(-0.4231, 0.2127)$	8.7426	$(-1.514, 0.2545)$
$M_{\text{EuS}}[\mu_{\text{B}}/\text{FU}]$ 6	5.1313	$(-0.1830, 0.6216)$	6.6916	$(-0.8133, 2.869 \cdot 10^{-2})$
$M_{\text{EuS}}[\mu_{\text{B}}/\text{FU}]$ 7K	4.6863	$(-0.1723, 0.3726)$	6.2243	$(-1.470, 0.3526)$
$M_{\text{EuS}}[\mu_{\text{B}}/\text{FU}]$ 8K	4.7489	$(-0.1027, 0.5627)$	5.0381	$(-0.2041, 0.5129)$
$M_{\text{EuS}}[\mu_{\text{B}}/\text{FU}]$ 12K	4.7519	$(-0.3001, 0.4603)$	4.9123	$(-0.7769, 0.5395)$
$\sigma_{\text{M,InAs}}[\text{Å}]$ 2K	2.4103	$(-0.5213, 2.133)$	5.7250	$(-0.4058, 3.552)$
$\sigma_{\text{M,InAs}}[\text{Å}]$ 2K 0.25T	9.9999	$(-11.99, 9.502 \cdot 10^{-7})$	-1.9988	$(-1.196 \cdot 10^{-3}, 11.99)$
$\sigma_{\text{M,InAs}}[\text{Å}]$ 2K 1T	1.9661	$(-0.9056, 1.513)$	9.9048	$(-5.460, 9.177 \cdot 10^{-2})$
$\sigma_{\text{M,InAs}}[\text{Å}]$ 6K	9.9999	$(-6.310, 2.383 \cdot 10^{-7})$	9.9999	$(-4.243, 1.785 \cdot 10^{-5})$
$\sigma_{\text{M,InAs}}[\text{Å}]$ 7K	9.9999	$(-11.50, 1.875 \cdot 10^{-6})$	9.9999	$(-6.304, 7.093 \cdot 10^{-6})$
$\sigma_{\text{M,InAs}}[\text{Å}]$ 8K	9.9999	$(-6.005, 1.498 \cdot 10^{-8})$	4.9903	$(-1.127, 2.253)$
$\sigma_{\text{M,InAs}}[\text{Å}]$ 12K	-1.9812	$(-4.756 \cdot 10^{-3}, 11.99)$	2.6890	$(-4.686, 7.158)$
$d_{\text{M,InAs}}[\text{Å}]$	138.5551	$(-27.44, 2.253 \cdot 10^{-2})$	24.9999	$(-5.435, 8.245 \cdot 10^{-8})$
$M_{\text{InAs}}[\mu_{\text{B}}/\text{FU}]$ 2K	-1.3777	$(-0.4377, 0.5791)$	-2.2018	$(-0.5079, 0.9489)$
$M_{\text{InAs}}[\mu_{\text{B}}/\text{FU}]$ 2K, 0.25T	-3.4197	$(-0.4875, 0.1517)$	-4.9999	$(-6.748 \cdot 10^{-8}, 2.630)$
$M_{\text{InAs}}[\mu_{\text{B}}/\text{FU}]$ 2K, 1T	0.6679	$(-0.5739, 0.8884)$	0.1915	$(-0.2720, 0.9332)$
$M_{\text{InAs}}[\mu_{\text{B}}/\text{FU}]$ 6	-1.4675	$(-0.6323, 0.6500s)$	-2.9609	$(-0.4961, 1.072)$
$M_{\text{InAs}}[\mu_{\text{B}}/\text{FU}]$ 7K	-1.4881	$(-0.3466, 0.3405)$	-2.5878	$(-0.7607, 1.076)$
$M_{\text{InAs}}[\mu_{\text{B}}/\text{FU}]$ 8K	-1.6887	$(-0.3583, 0.4317)$	-1.1242	$(-0.7346, 0.7813)$
$M_{\text{InAs}}[\mu_{\text{B}}/\text{FU}]$ 12K	-0.0312	$(-0.4871, 0.3058)$	-0.6282	$(-0.9772, 0.8737)$
$\sigma_{\text{M,InAs−Sub}}[\text{Å}]$ 2K	64.3908	$(-22.94, 5.258)$	9.9999	$(-9.997, 3.858 \cdot 10^{-6})$
$\sigma_{\text{M,InAs−Sub}}[\text{Å}]$ 2K 0.25T	69.9999	$(-68.86, 1.359 \cdot 10^{-5})$	9.9999	$(-9.996, 4.283 \cdot 10^{-7})$
$\sigma_{\text{M,InAs−Sub}}[\text{Å}]$ 2K 1T	69.9999	$(-69.97, 9.649 \cdot 10^{-5})$	9.9999	$(-9.998, 2.893 \cdot 10^{-5})$
$\sigma_{\text{M,InAs−Sub}}[\text{Å}]$ 6K	59.6864	$(-6.537, 6.392)$	9.9999	$(-10.00, 2.665 \cdot 10^{-6})$
$\sigma_{\text{M,InAs−Sub}}[\text{Å}]$ 7K	63.4830	$(-63.35, 6.517)$	9.9999	$(-10.00, 7.413 \cdot 10^{-6})$
$\sigma_{\text{M,InAs−Sub}}[\text{Å}]$ 8K	66.6448	$(-41.25, 3.140)$	9.9999	$(-9.993, 7.586 \cdot 10^{-7})$
$\sigma_{\text{M,InAs−Sub}}[\text{Å}]$ 12K	69.9982	$(-70.00, 1.745 \cdot 10^{-3})$	0.0197	$(-1.972 \cdot 10^{-2}, 9.969)$

Table 6.5: The fitted parameter values for model 4 for Qdev1001.

With a model of the system, a scattering length density through out the system can be determined, these are a bit easier to compare which gives us a more visual representation of our the parameters the model, an example of which can be seen in fig. 6.5, where we have plotted the SLD, as a function of the depth (z), of the sample.
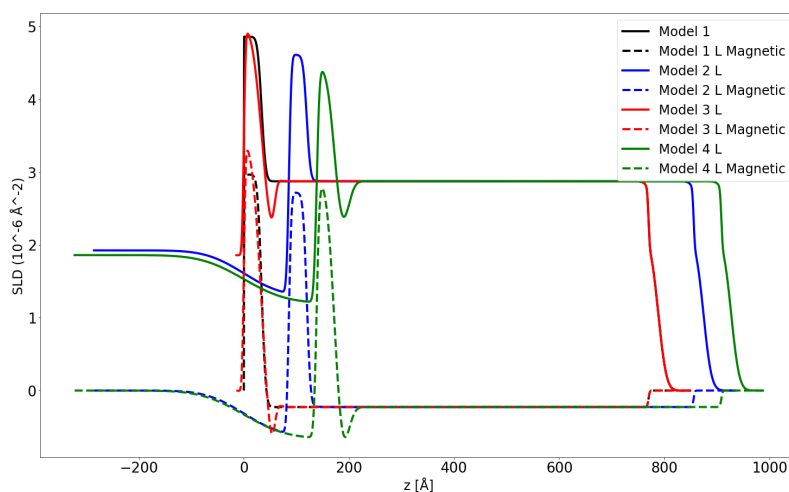
Figure 6.5: SLD for the different models of sample Qdev1001, at 2K. The solid lines are the total SLD, while the dashed lines are the magnetic SLD. We see can see that model 2 and 4 has a magnetization in the InAs layer. Note that the top of sample (Al_2O_3) start to the right of the plot, while the left of the plot is the bottom InAs, of the sample.

6.2 Qdev1002

The experiment on the sample Qdev1002, was conducted on POLREF, at ISIS by Y. Liu and Peter Krogstrup at University of Copenhagen, starting on 13/02/2020. The incident beam have a wavelength in the range $\lambda = 0.9$Å-15Å, which at the sample position have a beam area of $60\text{mm} \times 30\text{mm}$. Similar to before, the sample was mounted on a holder, then placed inside a cryomagnet, and aligned. Like before the measurement was done in an applied magnetic field of $B = 0.1$T. Measurements on the sample were taken at temperatures of 2.9K, 4K, 8K, 12K and 20K all at 0.1T.

6.2.1 Models and simulations

Like before we used GenX to determine the structure of the sample. This settings for the model of the instrument can be seen in fig. 6.7.

We fit our sample the same way we did Qdev1001. Starting with fitting the structure of the sample, from the 20K data. The result can be seen in table 6.6. Again the magnetic screening field is calculated by hand.

Next we fit our data to the 4 models that we test. Starting with model 1 where we assume that magnetization is only present in the EuS layer. These are fitted with the structure values we first found. The results can be seen in table 6.7, 6.8, 6.9 and 6.10 .
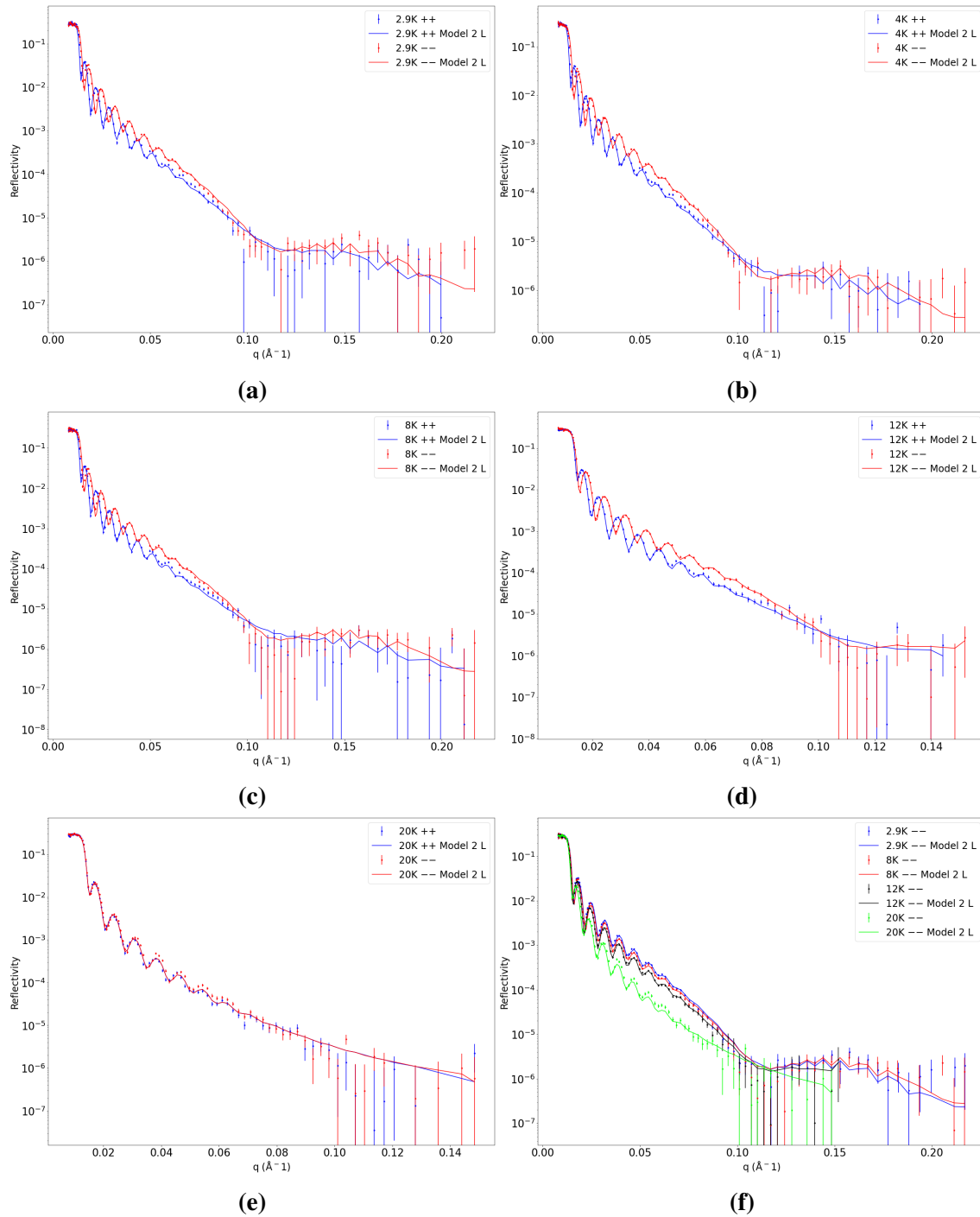
Figure 6.6: Plots of the data form the PNR experiment conducted on Qdev1002.
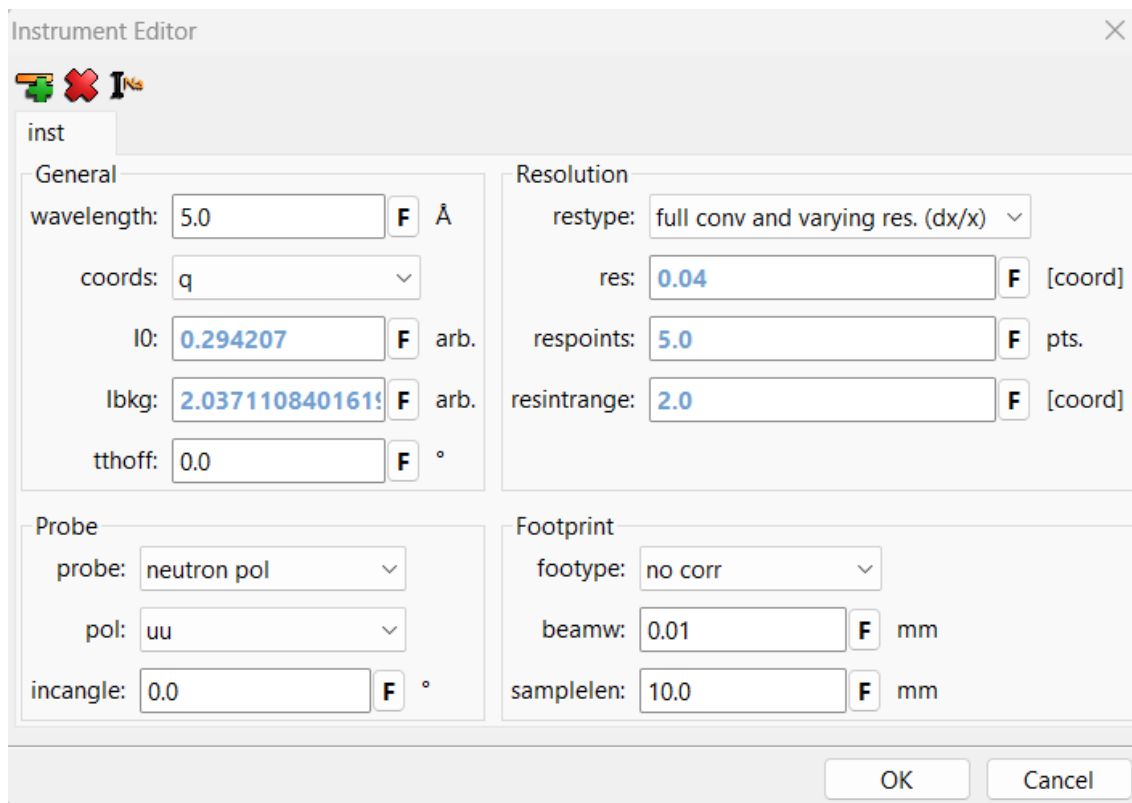
Figure 6.7: The instrument setting for our experiment on Qdev1002

Structure ($\chi^2 = 3.2937$)		
Parameter	Values	Error
$\sigma_{\text{Al}_2\text{O}_3}[\text{Å}]$	1.00	$(-3.843 \cdot 10^{-10}, 6.736)$
$d_{\text{Al}_2\text{O}_3}[\text{Å}]$	14.692	$(-2.265, 5.903)$
$b_{\text{Al}_2\text{O}_3}[\text{fm}]$	7.325	$(-2.265, 5.903)$
$\sigma_{\text{Pb}}[\text{Å}]$	2.00	$(-8.162 \cdot 10^{-11}, 7.826)$
$d_{\text{Pb}}[\text{Å}]$	758.918	$(-8.460, 5.190)$
$\sigma_{\text{EuS}}[\text{Å}]$	3.819	$(-1.775, 5.072)$
$d_{\text{EuS}}[\text{Å}]$	56.607	$(-10.21, 11.47)$
$\sigma_{\text{InAs}}[\text{Å}]$	2.0	$(-2.731 \cdot 10^{-10}, 7.988)$

Table 6.6: The structure values of Qdev1002. Note that this is only fitted from the data taken at 20K.

Model 1 ($\chi^2 = 9.1191$)		
Parameter	Values	Errors
$\sigma_{\mathrm{M,EuS}}[\mathring{\mathrm{A}}]$ 2.9K	4.7394	$(-6.610, 3.240)$
$\sigma_{\mathrm{M,EuS}}[\mathring{\mathrm{A}}]$ 4K	4.1371	$(-2.904, 4.106)$
$\sigma_{\mathrm{M,EuS}}[\mathring{\mathrm{A}}]$ 8K	3.2068	$(-2.696, 3.229)$
$\sigma_{\mathrm{M,EuS}}[\mathring{\mathrm{A}}]$ 12K	2.3164	$(-4.256, 6.668)$
$M_{\mathrm{EuS}}[\mu_{\mathrm{B}}/\mathrm{FU}]$ 2.9K	6.3244	$(-0.5465, 0.4743)$
$M_{\mathrm{EuS}}[\mu_{\mathrm{B}}/\mathrm{FU}]$ 4K	6.1513	$(-0.3737, -0.3784)$
$M_{\mathrm{EuS}}[\mu_{\mathrm{B}}/\mathrm{FU}]$ 8K	5.4302	$(-0.2673, 0.3251)$
$M_{\mathrm{EuS}}[\mu_{\mathrm{B}}/\mathrm{FU}]$ 12K	4.5595	$(-0.3648, 0.4540)$
$\sigma_{\mathrm{M,InAs}}[\mathring{\mathrm{A}}]$ 2.9K	-2.00	$(-1.598 \cdot 10^{-5}, 10.47)$
$\sigma_{\mathrm{M,InAs}}[\mathring{\mathrm{A}}]$ 4K	-2.00	$(-2.463 \cdot 10^{-5}, 10.98)$
$\sigma_{\mathrm{M,InAs}}[\mathring{\mathrm{A}}]$ 8K	-2.00	$(-4.234 \cdot 10^{-6}, 10.75)$
$\sigma_{\mathrm{M,InAs}}[\mathring{\mathrm{A}}]$ 12K	-2.00	$(-6.173 \cdot 10^{-6}, 11.99)$

Table 6.7: The fitted parameter values for model 1 for Qdev1002.

Model 2				
	Long Range ($\chi^2 = 7.0278$)		Short Range ($\chi^2 = 8.8348$)	
Parameter	Values	Errors	Values	Errors
$\sigma_{\text{M,EuS}}[\text{Å}]$ 2.9K	3.3255	$(-1.593, 1.755)$	7.3818	$(-5.836, 1.004)$
$\sigma_{\text{M,EuS}}[\text{Å}]$ 4K	3.4475	$(-1.984, 1.807)$	7.1607	$(-3.552, 2.287)$
$\sigma_{\text{M,EuS}}[\text{Å}]$ 8K	2.3345	$(-1.453, 1.510)$	7.3226	$(-4.411, 2.555)$
$\sigma_{\text{M,EuS}}[\text{Å}]$ 12K	2.4030	$(-2.798, 1.999)$	3.0919	$(-4.576, 4.458)$
$M_{\text{EuS}}[\mu_\text{B}/\text{FU}]$ 2.9K	5.3451	$(-0.4872, 0.5881)$	6.7353	$(-0.6038, 0.1900)$
$M_{\text{EuS}}[\mu_\text{B}/\text{FU}]$ 4K	5.1662	$(-0.3876, 0.5931)$	6.4593	$(-0.4450, 0.1228)$
$M_{\text{EuS}}[\mu_\text{B}/\text{FU}]$ 8K	4.3823	$(-0.3086, 0.2907)$	5.7678	$(-0.5010, 0.03356)$
$M_{\text{EuS}}[\mu_\text{B}/\text{FU}]$ 12K	4.5558	$(-0.2361, 0.3592)$	4.5766	$(-0.2020, 0.5303)$
$\sigma_{\text{M,InAs}}[\text{Å}]$ 2.9K	1.5501	$(-2.268, 4.324)$	6.6325	$(-8.520, 1.941)$
$\sigma_{\text{M,InAs}}[\text{Å}]$ 4K	-0.30959	$(-3.328, 3.801)$	5.3970	$(-8.420, 1.803)$
$\sigma_{\text{M,InAs}}[\text{Å}]$ 8K	-1.5513	$(-2.372, 3.694)$	6.5650	$(-9.734, 0.4413)$
$\sigma_{\text{M,InAs}}[\text{Å}]$ 12K	-4.0000	$(-1.994 \cdot 10^{-6}, 13.49)$	-3.9951	$(-4.867 \cdot 10^{-3}, 13.99)$
$d_{\text{M,InAs}}[\text{Å}]$	114.01	$(-35.53, 34.78)$	25.000	$(-17.09, 1.807 \cdot 10^{-7})$
$M_{\text{InAs}}[\mu_\text{B}/\text{FU}]$ 2.9K	-2.0707	$(-0.5524, 0.5930)$	-1.3996	$(-0.3685, 2.165)$
$M_{\text{InAs}}[\mu_\text{B}/\text{FU}]$ 4K	-2.0109	$(-0.5598, 0.4974)$	-1.3819	$(-0.7449, 1.038)$
$M_{\text{InAs}}[\mu_\text{B}/\text{FU}]$ 8K	-2.0745	$(-0.6951, 0.6060)$	-1.7007	$(-0.3514, 1.328)$
$M_{\text{InAs}}[\mu_\text{B}/\text{FU}]$ 12K	-0.017320	$(-0.4051, 0.3419)$	-0.12255	$(-1.588, 05847)$
$\sigma_{\text{M,InAs-Sub}}[\text{Å}]$ 2.9K	76.190	$(-22.70, 12.38)$	3.0000	$(-2.999, 2.089 \cdot 10^{-5})$
$\sigma_{\text{M,InAs-Sub}}[\text{Å}]$ 4K	75.900	$(-7.898, 7.891)$	3.0000	$(-2.998, 2.418 \cdot 10^{-5})$
$\sigma_{\text{M,InAs-Sub}}[\text{Å}]$ 8K	72.646	$(-24.23, 17.05)$	3.0000	$(-2.997, 4.670 \cdot 10^{-5})$
$\sigma_{\text{M,InAs-Sub}}[\text{Å}]$ 12K	90.000	$(-89.97, 1.031 \cdot 10^{-5})$	2.9999	$(-3.000, 1.229 \cdot 10^{-4})$

Table 6.8: The fitted parameter values for model 2 for Qdev1002.

Model 3					
	Long Range ($\chi^2 = 9.1278$)			Short Range ($\chi^2 = 9.4508$)	
Parameter	Values	Errors	Values	Errors	
$\sigma_{\mathrm{M,Pb}}[\mathrm{\mathring{A}}]$ 2.9K	0.0010	$(-1.069 \cdot 10^{-3}, 9.967))$	0.0065	$(-6.388 \cdot 10^{-3}, 9.991)$	
$\sigma_{\mathrm{M,Pb}}[\mathrm{\mathring{A}}]$ 4K	0.0030	$(-2.989 \cdot 10^{-3}, 9.986)$	6.9999	$(-6.994, 5.240 \cdot 10^{-5})$	
$\sigma_{\mathrm{M,Pb}}[\mathrm{\mathring{A}}]$ 8K	0.0023	$(-2.342 \cdot 10^{-3}, 9.997)$	6.9999	$(-6.998, 2.614 \cdot 10^{-5})$	
$\sigma_{\mathrm{M,Pb}}[\mathrm{\mathring{A}}]$ 12K	0.0106	$(-1.055 \cdot 10^{-2}, 9.988)$	6.9999	$(-7.000, 1.946 \cdot 10^{-5})$	
$d_{\mathrm{M,Pb}}[\mathrm{\mathring{A}}]$	42.9960	$(-17.22, 5.026)$	5.0000	$(-2.560 \cdot 10^{-5}, 14.41)$	
$M_{\mathrm{Pb}}[\mu_{\mathrm{B}}/\mathrm{FU}]$ 2.9K	-0.4085	$(-0.3547, 0.2777)$	0.5134	$(-1.666, 1.493)$	
$M_{\mathrm{Pb}}[\mu_{\mathrm{B}}/\mathrm{FU}]$ 4K	-0.4169	$(-0.4068, 0.3541)$	-0.5415	$(-1.866, 1.205)$	
$M_{\mathrm{Pb}}[\mu_{\mathrm{B}}/\mathrm{FU}]$ 8K	0.4533	$(-0.4029, 0.4284)$	-0.8057	$(-1.550, 1.410)$	
$M_{\mathrm{Pb}}[\mu_{\mathrm{B}}/\mathrm{FU}]$ 12K	-0.07349	$(-0.4026, 0.3178)$	-0.6580	$(-2.837, 1.855)$	
$\sigma_{\mathrm{M,EuS}}[\mathrm{\mathring{A}}]$ 2.9K	6.4039	$(-1.797, 1.009)$	4.3690	$(-3.141, 2.458)$	
$\sigma_{\mathrm{M,EuS}}[\mathrm{\mathring{A}}]$ 4K	5.8637	$(-4.759, 3.726)$	4.5482	$(-3.794, 2.640)$	
$\sigma_{\mathrm{M,EuS}}[\mathrm{\mathring{A}}]$ 8K	5.3052	$(-1.828, 2.814)$	3.9657	$(-3.076, 3.245)$	
$\sigma_{\mathrm{M,EuS}}[\mathrm{\mathring{A}}]$ 12K	3.9560	$(-2.253, 2.952)$	3.9221	$(-3.288, 3.928)$	
$M_{\mathrm{EuS}}[\mu_{\mathrm{B}}/\mathrm{FU}]$ 2.9K	6.3498	$(-0.2576, 0.3340)$	6.2406	$(-0.3030, 0.3622)$	
$M_{\mathrm{EuS}}[\mu_{\mathrm{B}}/\mathrm{FU}]$ 4K	6.1659	$(-0.4475, 0.3559)$	6.1849	$(-0.2901, 0.4040)$	
$M_{\mathrm{EuS}}[\mu_{\mathrm{B}}/\mathrm{FU}]$ 8K	5.4205	$(-0.3359, 0.417)$	5.4811	$(-0.3136, 0.5530)$	
$M_{\mathrm{EuS}}[\mu_{\mathrm{B}}/\mathrm{FU}]$ 12K	4.5866	$(-0.2168, 0.1992)$	4.6473	$(-0.1859, 0.3460)$	
$\sigma_{\mathrm{M,InAs}}[\mathrm{\mathring{A}}]$ 2.9K	-3.8707	$(-0.1265, 10.16)$	-3.9991	$(-8.343 \cdot 10^{-4}, 10.42)$	
$\sigma_{\mathrm{M,InAs}}[\mathrm{\mathring{A}}]$ 4K	-3.9999	$(-5.591 \cdot 10^{-6}, 10.99)$	-3.9997	$(-2.376 \cdot 10^{-4}, 10.39)$	
$\sigma_{\mathrm{M,InAs}}[\mathrm{\mathring{A}}]$ 8K	-3.9999	$(-1.954 \cdot 10^{-6}, 11.86)$	-3.9998	$(-1.187 \cdot 10^{-4}, 10.88$	
$\sigma_{\mathrm{M,InAs}}[\mathrm{\mathring{A}}]$ 12K	-3.9999	$(-1.840 \cdot 10^{-5}, 13.99)$	-3.9993	$(-6.814 \cdot 10^{-4}, 13.95)$	

Table 6.9: The fitted parameter values for model 3 for Qdev1002.

Model 4					
	Long Range ($\chi^2 = 6.4359$)			Short Range ($\chi^2 = 8.6691$)	
Parameter	Values	Errors		Values	Errors
$\sigma_{\mathrm{M,Pb}}[\text{Å}]$ 2.9K	17.726	$(-6.110, 2.356)$		7.9840	$(-7.983, 2.015)$
$\sigma_{\mathrm{M,Pb}}[\text{Å}]$ 4K	25.000	$(-24.99, 5.538 \cdot 10^{-7})$		9.8850	$(-9.884, 0.1150)$
$\sigma_{\mathrm{M,Pb}}[\text{Å}]$ 8K	25.000	$(-24.99, 1.454 \cdot 10^{-6})$		9.3454	$(-9.328, 0.6544)$
$\sigma_{\mathrm{M,Pb}}[\text{Å}]$ 12K	$2.8633 \cdot 10^{-3}$	$(-2.856 \cdot 10^{-3}, 24.98)$		9.9997	$(-0.1000, 2.060 \cdot 10^{-4})$
$d_{\mathrm{M,Pb}}[\text{Å}]$	45.065	$(-11.36, 11.77)$		4.0000	$(-9.677 \cdot 10^{-5}, 4.755)$
$M_{\mathrm{Pb}}[\mu_{\mathrm{B}}/\text{FU}]$ 2.9K	-0.85629	$(-0.1413, 0.2400)$		3.0064	$(-2.703, 0.3401)$
$M_{\mathrm{Pb}}[\mu_{\mathrm{B}}/\text{FU}]$ 4K	-0.88671	$(-0.2168, 0.4313)$		1.9022	$(-1.335, 0.9424)$
$M_{\mathrm{Pb}}[\mu_{\mathrm{B}}/\text{FU}]$ 8K	-0.97066	$(-0.1429, 0.2507)$		1.8902	$(-1.773, 0.7222)$
$M_{\mathrm{Pb}}[\mu_{\mathrm{B}}/\text{FU}]$ 12K	$-7.7654 \cdot 10^{-2}$	$(-0.2305, 0.2000)$		-0.8253	$(-1.506, 0.7190)$
$\sigma_{\mathrm{M,EuS}}[\text{Å}]$ 2.9K	7.6594	$(-3.969, 2.128)$		5.7116	$(-2.742, 2.433)$
$\sigma_{\mathrm{M,EuS}}[\text{Å}]$ 4K	7.2679	$(-2.093, 2.374)$		5.5900	$(-2.127, 2.014)$
$\sigma_{\mathrm{M,EuS}}[\text{Å}]$ 8K	6.7903	$(-1.484, 1.851)$		5.7094	$(-1.733, 3.631)$
$\sigma_{\mathrm{M,EuS}}[\text{Å}]$ 12K	4.0062	$(-2.218, 1.891)$		4.5920	$(-0.1275, 3.004)$
$M_{\mathrm{EuS}}[\mu_{\mathrm{B}}/\text{FU}]$ 2.9K	5.2287	$(-0.3280, 0.5129)$		6.1556	$(-0.1186, 0.2451)$
$M_{\mathrm{EuS}}[\mu_{\mathrm{B}}/\text{FU}]$ 4K	4.9589	$(-0.2080, 0.3117)$		6.0885	$(-0.2294, 0.1404)$
$M_{\mathrm{EuS}}[\mu_{\mathrm{B}}/\text{FU}]$ 8K	4.1408	$(-0.1264, 0.2758)$		5.3585	$(-0.1887, 0.4013)$
$M_{\mathrm{EuS}}[\mu_{\mathrm{B}}/\text{FU}]$ 12K	4.5598	$(-0.1264, 0.2758)$		4.6642	$(-5.380 \cdot 10^{-2}, 0.4726)$
$\sigma_{\mathrm{M,InAs}}[\text{Å}]$ 2.9K	2.6665	$(-2.864, 2.278)$		3.9876	$(-6.864, 1.335)$
$\sigma_{\mathrm{M,InAs}}[\text{Å}]$ 4K	0.31180	$(-3.662, 3.781)$		3.2587	$(-4.840, 3.410)$
$\sigma_{\mathrm{M,InAs}}[\text{Å}]$ 8K	-0.42566	$(-2.420, 2.438)$		4.5033	$(-3.913, 2.248)$
$\sigma_{\mathrm{M,InAs}}[\text{Å}]$ 12K	-4.0000	$(-1.252 \cdot 10^{-5}, 13.29)$		-1.0841	$(-2.912, 8.408)$
$d_{\mathrm{M,InAs}}[\text{Å}]$	150.05	$(-29.55, 17.33)$		24.9999	$(-18.94, 4.649 \cdot 10^{-6})$
$M_{\mathrm{InAs}}[\mu_{\mathrm{B}}/\text{FU}]$ 2.9K	-2.1943	$(-0.5452, 0.7243)$		-1.5293	$(-2.496, 1.088)$
$M_{\mathrm{InAs}}[\mu_{\mathrm{B}}/\text{FU}]$ 4K	-2.1661	$(-0.3998, 0.3413)$		-1.5532	$(-2.253, 0.8374)$
$M_{\mathrm{InAs}}[\mu_{\mathrm{B}}/\text{FU}]$ 8K	-2.1789	$(-0.3018, 0.3725)$		-1.8880	$(-2.858, 6.358)$
$M_{\mathrm{InAs}}[\mu_{\mathrm{B}}/\text{FU}]$ 12K	$-5.4001 \cdot 10^{-2}$	$(-0.2426, 0.2227)$		-0.1258	$(-1.945, 0.9187)$
$\sigma_{\mathrm{M,InAs-Sub}}[\text{Å}]$ 2.9K	68.243	$(-10.90, 10.06)$		9.9999	$(-9.995, 7.650 \cdot 10^{-6})$
$\sigma_{\mathrm{M,InAs-Sub}}[\text{Å}]$ 4K	68.453	$(-14.29, 13.84)$		9.9999	$(-9.995, 2.002 \cdot 10^{-5})$
$\sigma_{\mathrm{M,InAs-Sub}}[\text{Å}]$ 8K	62.409	$(-10.43, 10.34)$		9.9999	$(-9.999, 3.757 \cdot 10^{-7})$
$\sigma_{\mathrm{M,InAs-Sub}}[\text{Å}]$ 12K	90.000	$(-8.997, 1.457 \cdot 10^{-5})$		9.9998	$(-9.999, 1.002 \cdot 10^{-4})$

Table 6.10: The fitted parameter values for model 4 for Qdev1002.

7 Discussion

In this chapter, we will discuss the result of the previous section. We will be comparing the 4 models, to see which one fit the best with our data. Afterwards, we will look at the best model, and try and determine what we actually see.

7.1   Qdev1001

We start by looking at the χ^2 values of our fitted models for the sample Qdev1001. These can be found in table 7.1. From these we can quickly see two things. First, that we can discard model 1 and 3, (see fig 6.4 for reference), as their χ^2 values are significantly higher than the ones for model 2 and 4. Similarly, for the model 2 and 4, we can then see that the proximity effect is long range rather than short range, based on the χ^2 values, combined with the fact, that in the short range fits, the thickness reaches the maximum allowed value, of 25Å. Now to compare in between models 2 and 4, it should be noted that although model 4, perform slightly better than model 2, there are extra degrees of freedom included in model 4. Therefore we will say that small difference in χ^2 value, is simply not enough to justify it. Based on this discussion, we can argue that the magnetic and crystal structure associated with model 2 provides the best resemblance to our experimental results.

χ^2 values		
Model	Long range	Short range
Structure	4.7267	
Model 1	50.095 (27.689)	
Model 2	37.936 (23.228)	44.730 (26.558)
Model 3	51.276 (31.629)	52.095 (32.112)
Model 4	37.838 (26.047)	47.483 (29.114)

Table 7.1: The chi-square values of the fits, for Qdev1001. The structure fit, is the one where we fitted the data taken at 20K, 50K and 300K. The values in parenthesis are the values excluding the data taken, with an applied B-field of 0.25T.

The question now, is of course what exactly our model shows. We start by looking at the magnetization in the EuS layer, see table 6.3. As we have discussed previously, the Curie

temperature of EuS, is $T_c \sim 16.5\text{K}$, and the superconducting ordering temperature of Pb, is $T_s \sim 7\text{K}$, but while lead is normally a type 1 superconductor which has a sharp transition at superconducting ordering temperature, but as we have mentioned before, in the thin limit it behaves more like a type 2 superconductor, which has a more gradual transition. At 12K, where we are below the Curie temperature of EuS, but not yet at a temperature where the there should be magnetic saturation, we get a magnetization of $M_{12\text{K}} = 4.3453\mu_{\text{B}}/\text{FU}$. Looking at the result for 2K, where we should have reached magnetic saturation, we have a magnetization of $M_{2\text{K}} = 5.4122\mu_{\text{B}}/\text{FU}$, in the presence of an 0.1T applied magnetic field. Looking at the rest of the data though, we see something interesting. The first thing is that, when we decrease the temperature from 12K to 2K, the value for the magnetization at 12, 8K, 7K and 6K, are $M_{12\text{K}} = 4.3453$, $M_{8\text{K}} = 4.0844\mu_{\text{B}}/\text{FU}$, $M_{7\text{K}} = 4.2367\mu_{\text{B}}/\text{FU}$ and $M_{6\text{K}} = 4.5334\mu_{\text{B}}/\text{FU}$. Now from this, it seems like there is a suppression of the magnetization from the superconductor, near the ordering temperature of lead. To confirm this behavior, we have done the experiment in presence of a 1T applied magnetic field, which is higher than the critical magnetic field of lead. We observe an EuS magnetization of $M_{2\text{K},1\text{T}} = 6.7889\mu_{\text{B}}/\text{FU}$. This shows clearly, that when we are in a state where lead is not in superconducting state, we see an increase in the magnetization of EuS at 2K. Both of these results indicates, that the superconductivity of lead, modifies the magnetization in the EuS layer.

Turning now to the InAs layer, we see again, that the superconductivity, seem to affect the magnetization. From the fit we get that there should be a magnetic layer of thickness $d_{\text{M,InAs}} = 85.842\text{Å}$ where the magnetization is decreasing when we go deeper in the InAs layer, as can be seen from fig 7.1, and from the large values of the magnetic roughness. Interestingly we have seen the effect of superconducting ordering in the values of the InAs magnetization. The values of the InAs magnetization when the lead is in the superconducting, that is 8K, 7K, 6K , and 2K, are $M_{\text{InAs,8K}} = -1.5473\mu_{\text{B}}/\text{FU}$, $M_{\text{InAs,7K}} = -1.3090\mu_{\text{B}}/\text{FU}$, $M_{\text{InAs,6K}} = -1.2800\mu_{\text{B}}/\text{FU}$ and $M_{\text{InAs,2K}} = -1.1378\mu_{\text{B}}/\text{FU}$. Whereas the values of the InAs magnetization when lead is not in the superconducting state, that is 12K and 2K with an 1T applied field, are $M_{\text{InAs,12K}} = 0.12692\mu_{\text{B}}/\text{FU}$ and $M_{\text{InAs,2K,1T}} = 0.99328\mu_{\text{B}}/\text{FU}$. The thing of note is of course the negative values, which indicates a magnetization opposite to the one in the EuS layer, and which are only present in a superconducting regime. A plot of the magnetization values can be seen in fig 7.2(a).

Now it is worth mentioning that we have not included the data taken at 2K with an applied B-field of 0.25T. But looking at it, we see that we get result that are very different, and seemingly unrelated to the other data, such as the magnetization in EuS being $M_{2\text{K},0.25\text{T}} = 3\mu_{\text{B}}/\text{FU}$. The probable explanation for this, is that the data for 0.25T only goes up to
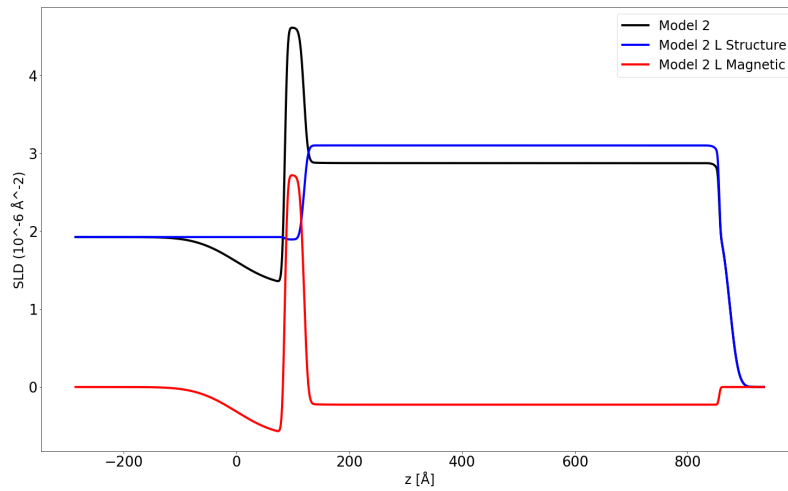
Figure 7.1: SLD for model 2 at 2K. We can clearly see that the magnetization decreases as we go deeper into the InAs layer.

q-values around 0.08Å^{-1} while the rest of the data goes to around 0.2Å^{-1}. This means the data is no very useful, or reliable, as what we are looking for is more observable at larger q-values. The result of the this can be seen in fig. 6.2i which shows that the data for 0.25T is not fitted very well. In fact if we discard the 0.25T data, as can be done without affecting the result of our fits, we get markedly improved χ^2 values, for all our models.
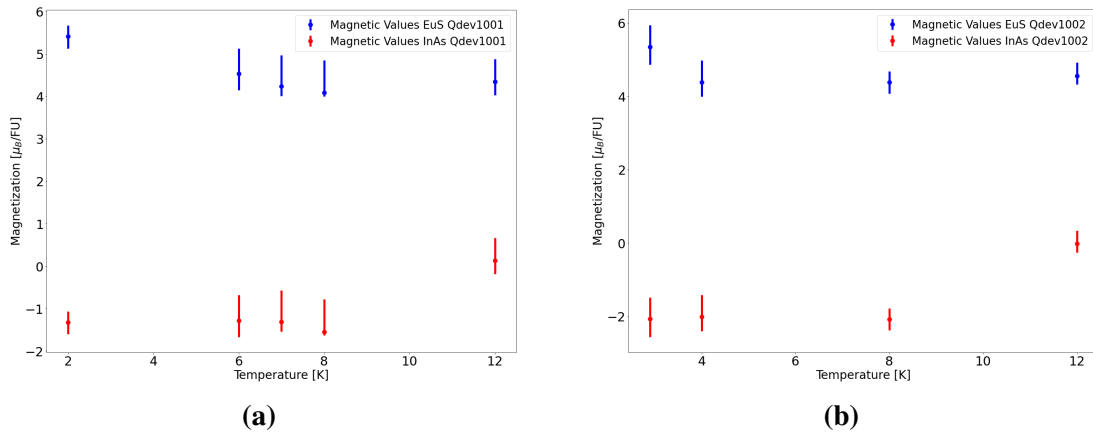

Figure 7.2: The values of the magnetization in EuS and InAs for our two samples, (a) Qdev1001 and (b) Qdev1002

7.2 Qdev1002

We now turn to the sample Qdev1002. Similar to Qdev1001, we can discard model 1 and model 3, and we can choose the long range models, based on the χ^2 values, see table 7.2. Here we again also see a slightly smaller χ^2 value for model 4, than for model 2, but again

57

because of the increased number of degrees of freedom, we will choose model 2. While we do not have any data for an applied B-field larger than 0.1T, we do see the same suppression in the magnetization in the EuS layer, as we enter the superconducting regime. Again we also see a magnetic layer in InAs, here with a thickness of $d_{\mathrm{M,InAs}} = 114.01$Å. Now in Qdev1002 we do see a slight difference in comparison to the results of Qdev1001. While we still get a magnetization in the InAs layer, with direction opposite to the magnetization in the EuS layer, in the superconducting regime, it is here larger than the one we see in Qdev1001. Furthermore, while the InAs layer in Qdev1001, had a magnetization of almost $1\mu_{\mathrm{B}}/\mathrm{FU}$ at 12K, in the same direction as the magnetization in EuS, here it is, $M_{\mathrm{InAS,12K}} = -0.017320\mu_{\mathrm{B}}/\mathrm{FU}$, opposite the direction in the EuS layer, and very small. A plot of the magnetization values can be seen in fig. 7.2(b).

χ^2 values		
Model	Long range	Short range
Structure	3.2937	
Model 1	9.1191	
Model 2	7.0278	8.8348
Model 3	9.1278	9.4508
Model 4	6.4359	8.6691

Table 7.2: The chi-square values of the fits, for Qdev1002 The structure fit, is the one where we fitted the data taken at 20K.

Comparing the two samples, it is difficult to say what exactly is the cause for the difference, but it is presumably related to the different thicknesses of the their EuS layer, especially the fact that Qdev1001 has a thickness that is smaller than the superconducting coherence length of lead $\xi_{Pb} = 39$nm while Qdev1002 has ans a thickness that is larger than the coherence length, and the roughness of their interfaces, is very similar. We can however say, that in both of them, we see the presence of a magnetic field in the InAs layer, which seems to be affected by the superconductivity of the lead layer. Now whether this is related to a spin-asymmetric tunneling from the lead layer into the InAs layer, as suggested in [33], or something different, is difficult to say. Moreover it seems clear that we have magnetization outside the EuS layer, and that it is not just related to the magnetization of the EuS layer, but also affected by the superconductivity.

8 Conclusion

We have investigated semiconductor-ferromagnetic insulator-superconductor (SM-FMI-SC) heterostructures, to explore the possibility of magnetic proximity effect at the SC-FMI and the FMI-SM interfaces.

In the present work, we have used molecular beam epitaxy grown samples InAs(substrate)-EuS-Pb(70nm)-Al$_2$O$_3$(2nm), where the EuS thicknesses are varied. Polarized neutron reflectometry is used to determine the layer structure as well as to understand how the depth profile of the magnetization changes across the magnetic and superconducting ordering temperatures.

The ferromagnetic ordering temperature for EuS is 16.5K and the superconducting transition temperature for Pb is 7.2K. We have used PNR data at temperature values above both the ordering temperatures (T = 20K, 50K, 300K) to determine the thickness and roughness of the individual layers. We have further recorded PNR data while sweeping the temperature in a close range of ordering transitions of EuS and Pb and, varying the applied magnetic field value across the critical field of superconducting Pb. The measured data is analyzed by comparing the experimental reflectivity profiles with the simulated profiles generated from different possible magnetic structures and, the χ^2 values are used to determine the most suitable magnetic model.

We have noticed that the magnetization in the EuS layer was affected by the presence of superconductivity in the Pb layer. We observed a significant decrease in EuS magnetization during the onset of superconductivity in Pb at 8K. We further observed that the saturated EuS magnetization (T = 2K) was enhanced from $M_{\mathrm{EuS}} = 5.4122\mu_{\mathrm{B}}/\mathrm{FU}$ to $M_{\mathrm{EuS}} = 6.7889\mu_{\mathrm{B}}/\mathrm{FU}$, when applied field was increased beyond the critical field of superconducting Pb. We also saw that this effect does not seem to be dependent on the thickness of the EuS layer.

Furthermore, we noticed the presence of induced magnetization in the InAs layer, which was affected by both the thickness of the EuS layer, and the superconductivity in the Pb layer. In first sample, with EuS thickness of $d_{\mathrm{EuS}} \sim 3.4$nm, we noticed a magnetic layer in the InAs, with thickness of $d_{\mathrm{InAs}} \sim 8.5$nm, while in the second sample, with an EuS layer of thickness $d_{\mathrm{EuS}} \sim 5.6$nm, we observed a magnetic layer in the InAs of

thickness $d_{\mathrm{InAs}} \sim 11.4\mathrm{nm}$. We found that, when Pb is superconducting, the magnetization in the InAs layer is oriented along the opposite direction of the magnetization in the EuS, for both of the samples. However, for the temperature and field values when Pb is not superconducting, we observed that the two samples behave differently. For the first sample with thinner EuS layer ($d_{\mathrm{EuS}} \sim 3.4\mathrm{nm}$), the magnetization is orientated in the same direction as the magnetization in the EuS layer, whereas for the second sample with a thicker EuS layer($d_{\mathrm{EuS}} \sim 5.6\mathrm{nm}$), the magnetization remains oppositly aligned with respect to the magnetization in the EuS layer. These results are aligned with the possibility of spin-asymmetric tunnelling from superconducting Pb layer into InAs layer, as described in ref [33].

8.1 Outlook

As we have determined that there is magnetization in the semiconducting layer of our heterostructure that seem to be affected by the presence of superconductivity, it seems logical to examine this effect in the temperature range slightly above the critical temperature, to determine whether the superconductivity actually affects this proximity effect. In the same manner would it be helpful to collect data with an applied magnetic field with varying values around the superconducting critical field. It would furthermore be of interest to investigate SC-SM-FMI-SM heterostructures to compare the difference. At last, in order to take more clear data, that would make it easier to distinguish between the potential models, it would be helpful to create multilayer version of our SC-FMI-SM hetereostructure, as that will make the contrast more clear. Last as we have only done specular non spin-flip reflectometry on out sample, which can only determine the part of the magnetization that is in the plane of the sample, it would be useful to use spin-flip reflectometry, as is can determine the magnetization perpendicular to the surface. From a theoretical perspective, it would be helpful, to have a numerical Green's function analysis of the our system.

Bibliography

[1] Institut laue langevin. `https://www.ill.eu/`.

[2] Isis neutron and muon source. `https://www.isis.stfc.ac.uk/Pages/home.aspx`.

[3] There's plenty of room at the bottom. Lecture given by Richard Feynman at Caltech Institute of Technology on December 29, 1959.

[4] R. Aguado. Majorana quasiparticles in condensed matter. *Rivista del Nuovo Cimento*, 40, 10 2017.

[5] Jason Alicea. Majorana fermions in a tunable semiconductor device. *Phys. Rev. B*, 81:125318, Mar 2010.

[6] J. F. Annett. *Superconductivity, Superfluids, and Condensates*. Oxford University Press, 2004.

[7] J. Bardeen, L. N. Cooper, and J. R. Schrieffer. Theory of superconductivity. *Phys. Rev.*, 108:1175–1204, Dec 1957.

[8] F. S. Bergeret, A. F. Volkov, and K. B. Efetov. Induced ferromagnetism due to superconductivity in superconductor-ferromagnet structures. *Phys. Rev. B*, 69:174504, May 2004.

[9] F. S. Bergeret, A. Levy Yeyati, and A. Martín-Rodero. Inverse proximity effect in superconductor-ferromagnet structures: From the ballistic to the diffusive limit. *Phys. Rev. B*, 72:064524, Aug 2005.

[10] F. Sebastian Bergeret, Mikhail Silaev, Pauli Virtanen, and Tero T. Heikkilä. Colloquium: Nonequilibrium effects in superconductors with a spin-splitting field. *Rev. Mod. Phys.*, 90:041001, Oct 2018.

[11] Matts Björck and Gabriella Andersson. Genx: An extensible x-ray reflectivity refinement program utilizing differential evolution. *Journal of Applied Crystallography - J APPL CRYST*, 40:1174–1178, 12 2007.

[12] S Blundell. *The Theory of Magnetism Made Simple - An Introduction to Physical Concepts and to Some Useful Mathematical Methods*. World Scientific Publishing Co. Pte. Ltd., 2006.

[13] A. I. Buzdin. Proximity effects in superconductor-ferromagnet heterostructures. *Rev. Mod. Phys.*, 77:935–976, Sep 2005.

[14] G. Chanin and J. P. Torre. Critical-field curve of superconducting lead. *Phys. Rev. B*, 5:4357–4364, Jun 1972.

[15] Robert Cubitt and Giovanna Fragneto. Chapter 2.8.3 - neutron reflection:: Principles and examples of applications. In Roy Pike and Pierre Sabatier, editors, *Scattering*, pages 1198–1208. Academic Press, London, 2002.

[16] P. G. DE GENNES. Boundary effects in superconductors. *Rev. Mod. Phys.*, 36:225–237, Jan 1964.

[17] K. Fossheim and A. Sudbø. *Superconductivity: Physics and Applications*. John Wiley Sons Ltd, 2004.

[18] X. Hao, J. S. Moodera, and R. Meservey. Spin-filter effect of ferromagnetic europium sulfide tunnel barriers. *Phys. Rev. B*, 42:8235–8243, Nov 1990.

[19] Alberto Hijano, Stefan Ilić, Mikel Rouco, Carmen González-Orellana, Maxim Ilyn, Celia Rogero, P. Virtanen, T. T. Heikkilä, S. Khorshidian, M. Spies, N. Ligato, F. Giazotto, E. Strambini, and F. Sebastián Bergeret. Coexistence of superconductivity and spin-splitting fields in superconductor/ferromagnetic insulator bilayers of arbitrary thickness. *Phys. Rev. Research*, 3:023131, May 2021.

[20] Yurii A Izyumov, Yurii N Proshin, and Mensur G Khusainov. Competition between superconductivity and magnetism in ferromagnet/superconductor heterostructure. *Phys.-Usp.*, 45:109, 2002.

[21] G.P. Felcher J.F. Ankner. Polarized-neutron reflectometry. *Journal of Magnetism and Magnetic Materials*, 200:741–754, 1999.

[22] S. Langridge J.P. Goff, J.A.C. Bland and R.M. Dalgliesh. Polref science case, internal document.

[23] M. Yu. Kharitonov, A. F. Volkov, and K. B. Efetov. Oscillations of induced magnetization in superconductor-ferromagnet heterostructures. *Phys. Rev. B*, 73:054511, Feb 2006.

[24] A Yu Kitaev. Unpaired majorana fermions in quantum wires. *Phys.-Usp*, 44 131, 2001.

[25] C. Kittel. *Introduction to Solid State Physics*. John Wiley Sons, Inc, 8 edition, 2005.

[26] Vladimir Z. Kresin, Hans Morawitz, and Stuart A. Wolf. *Superconducting State: Mechanisms and Properties*. Oxford Scholarship Online, 2013.

[27] K. Lefmann. *Neutron Scattering: Theory, Instrumentation, and Simulation*. Niels Bohr Institute, University of Copenhagen, 2017.

[28] Jacob Linder, Takehito Yokoyama, and Asle Sudbø. Theory of superconducting and magnetic proximity effect in s/f structures with inhomogeneous magnetization textures and spin-active interfaces. *Phys. Rev. B*, 79:054523, Feb 2009.

[29] Yu Liu, Alessandra Luchini, Sara Martí-Sánchez, Christian Koch, Sergej Schuwalow, Sabbir A. Khan, Tomaš Stankevič, Sonia Francoual, Jose R. L. Mardegan, Jonas A. Krieger, Vladimir N. Strocov, Jochen Stahn, Carlos A. F. Vaz, Mahesh Ramakrishnan, Urs Staub, Kim Lefmann, Gabriel Aeppli, Jordi Arbiol, and Peter Krogstrup. Coherent epitaxial semiconductor–ferromagnetic insulator inas/eus interfaces: Band alignment and magnetic structure. *ACS Applied Materials & Interfaces*, 12(7):8780–8787, 2020. PMID: 31877013.

[30] A. Luchini. Neutron reflectometry - structural biophysics x ray and neutron scattering.

[31] Getzlaff M. *Fundamentals of Magnetism*. Springer, 2008.

[32] K. Flesnberg M. Leijnse. Introduction to topological superconductivity and majorana fermions. *Semicond. Sci. Technol*, 27 124003, 2012.

[33] A. Maiani, R. Seoane Souto, M. Leijnse, and K. Flensberg. Topological superconductivity in semiconductor–superconductor–magnetic-insulator heterostructures. *Phys. Rev. B*, 103:104508, Mar 2021.

[34] W. L. McMillan. Tunneling model of the superconducting proximity effect. *Phys. Rev.*, 175:537–542, Nov 1968.

[35] S. Mironov, A. S. Mel'nikov, and A. Buzdin. Electromagnetic proximity effect in planar superconductor-ferromagnet structures. *Applied Physics Letters*, 113(2):022601, 2018.

[36] Névot, L. and Croce, P. Caractérisation des surfaces par réflexion rasante de rayons x. application à l'étude du polissage de quelques verres silicates. *Rev. Phys. Appl. (Paris)*, 15(3):761–779, 1980.

[37] Christopher R. Reeg and Dmitrii L. Maslov. Hard gap in a normal layer coupled to a superconductor. *Phys. Rev. B*, 94:020501, Jul 2016.

[38] Cong Ren, J. Trbovic, R. L. Kallaher, J. G. Braden, J. S. Parker, S. von Molnár, and P. Xiong. Measurement of the spin polarization of the magnetic semiconductor EuS with zero-field and zeeman-split andreev reflection spectroscopy. *Phys. Rev. B*, 75:205208, May 2007.

[39] Blundell S. *Magnetism in Condensed Matter*. Oxford University Press, 2001.

[40] Thomas Saerbeck, Robert Cubitt, Andrew Wildes, Giuliana Manzin, Ken H. Andersen, and Philipp Gutfreund. Recent upgrades of the neutron reflectometer D17 at ILL. *Journal of Applied Crystallography*, 51(2):249–256, Apr 2018.

[41] Jay D. Sau, Roman M. Lutchyn, Sumanta Tewari, and S. Das Sarma. Generic new platform for topological quantum computation using semiconductor heterostructures. *Phys. Rev. Lett.*, 104:040502, Jan 2010.

[42] Jay D. Sau, Sumanta Tewari, Roman M. Lutchyn, Tudor D. Stanescu, and S. Das Sarma. Non-abelian quantum order in spin-orbit-coupled semiconductors: Search for topological majorana particles in solid-state systems. *Phys. Rev. B*, 82:214509, Dec 2010.

[43] Varley F. Sears. Neutron scattering lengths and cross sections. *Neutron News*, 3(3):26–37, 1992.

[44] J. Stahn, J. Chakhalian, Ch. Niedermayer, J. Hoppler, T. Gutberlet, J. Voigt, F. Treubel, H-U. Habermeier, G. Cristiani, B. Keimer, and C. Bernhard. Magnetic proximity effect in perovskite superconductor/ferromagnet multilayers. *Phys. Rev. B*, 71:140509, Apr 2005.

[45] E. Strambini, V. N. Golovach, G. De Simoni, J. S. Moodera, F. S. Bergeret, and F. Giazotto. Revealing the magnetic proximity effect in eus/al bilayers through superconducting tunneling spectroscopy. *Phys. Rev. Materials*, 1:054402, Oct 2017.

[46] P. M. Tedrow, J. E. Tkaczyk, and A. Kumar. Spin-polarized electron tunneling study of an artificially layered superconductor with internal magnetic field: Euo-al. *Phys. Rev. Lett.*, 56:1746–1749, Apr 1986.

[47] C. Timm. *Theory of Superconductivity*. Institute of Theoretical Physics, TU Dresden, 2022.

[48] T. Tokuyasu, J. A. Sauls, and D. Rainer. Proximity effect of a ferromagnetic insulator in contact with a superconductor. *Phys. Rev. B*, 38:8823–8833, Nov 1988.

[49] E. Tsymbal. Evaluation of the magnetic dipolar fields from layered systems on atomic scale. *Journal of Magnetism and Magnetic Materials*, 130(1):L6–L12, 1994.

[50] Weiss, Pierre. L'hypothèse du champ moléculaire et la propriété ferromagnétique. *J. Phys. Theor. Appl.*, 6(1):661–690, 1907.

[51] M. J. Wolf, C. Sürgers, G. Fischer, and D. Beckmann. Spin-polarized quasiparticle transport in exchange-split superconducting aluminum on europium sulfide. *Phys. Rev. B*, 90:144509, Oct 2014.

[52] V. O. Yagovtsev, N. A. Gusev, N. G. Pugach, and M. Eschrig. The inverse proximity effect in strong ferromagnet–superconductor structures. *Supercond. Sci. Technol.*, 34, Jan 2021.

[53] Yimei Zhu, editor. *Application of polarized neutron reflectometry to studies of artificially structured magnetic materials*, pages 107–155. Springer US, Boston, MA, 2005.